Title

Heat flow scaling relationships for the glass-ceiling convective regime and implications for Venus

Journal
Geodynamica, 1(1)

ISSN
3065-2804

Authors
Kerr, Madeleine
Stegman, Dave
Smrekar, Suzanne

Publication Date
2026-08-13

DOI
10.5070/F3.52916

Research Article

geodynamica

Heat flow and velocity scaling in the "glass-ceiling" convective regime and implications for Venus

Madeleine C. Kerr *[1,2], **Dave R. Stegman** [2], **Suzanne E. Smrekar** [3]

[1] *Earth, Planetary and Space Sciences Department, University of California Los Angeles, Los Angeles CA, USA*
[2] *Institute of Geophysics and Planetary Physics, Scripps Institution of Oceanography, University of California San Diego, La Jolla CA, USA*
[3] *Jet Propulsion Laboratory, California Institute of Technology, Pasadena CA, USA*

Abstract

Several rocky bodies in our Solar System, and perhaps the planet Venus, appear to operate in a stagnant lid tectonic regime. Therefore, understanding in sufficient detail how mantle convection operates under this mode of tectonics is essential to understanding our Solar System and potentially other extrasolar rocky bodies. Stagnant lid planets with sub-solidus internal temperature can have lower surface heat flows than mobile lid planets like Earth. However, Earth-like surface heat flows and high degrees of variability have been inferred from elastic lithosphere thickness estimates for Venus, leading researchers to wonder how these higher heat fluxes occur. Mineral phase transitions in the upper mantle can inhibit or enhance mass exchange through the mantle transition zone at pressures and temperatures relevant for larger terrestrial mantles such as those of Earth or Venus. This study explores how the endothermic wadsleyite to majorite plus ferropericlase transition (hereafter, WMF transition or WMF zone) demonstrates weaker upper-lower mantle layering for increasingly higher Rayleigh numbers and higher mantle temperatures. This counterintuitive weakening induces more numerous and continuous flushing events (mantle avalanches) between the upper and lower mantle, defining a convective regime we call the "glass-ceiling" and inducing a state of sustained, higher-efficiency heat flow throughout the mantle. This state manifests as a "jump" or upwards shift in the classical Rayleigh-Nusselt scaling compared to colder models outside of the WMF zone. A higher efficiency state of continuously-layered-and-flushed stagnant lid convection may be relevant for Venus which lacks apparent plate tectonics yet has regions which show evidence of short-wavelength variability and locally-high Earth-like surface heat fluxes. This dynamical effect may work in concert with melt-induced heat flow and lithospheric thinning to explain the present-day state of Venus' surface.

Editor(s):
Julien Monteux
Nicolas Flament
Iris van Zelst
Production:
Arushi Saxena
Mandy Bethkenhagen

Reviewers:
Gaël Choblet
Carianna Herrera

Submitted:
30 September 2025
Accepted:
18 May 2026
Published:
16 August 2026

1 Introduction

Venus is the planet in the Solar System most like Earth in terms of its size, distance from the Sun, and bulk density. However, the planet does not exhibit a system of plate tectonics like Earth which move at rates of 100 mm/yr or higher to transport cold lithosphere from the surface into the deep interior of the planet at subduction zones. Instead, Venus exhibits a single, connected lithosphere with only a few regions evocative of Earth-like subduction zones (*Sandwell and Schubert*, 1992; *Adams et al.*, 2023). More broadly, stagnant lid convection is a regime of solid-state mantle convection relevant for many other planets and moons in our Solar System (*Solomatov*, 1995; *Solomatov and Moresi*, 2000; *Michaut et al.*, 2025). It is characterized by the strong temperature-dependent viscosity of planetary mantle silicates. This exponential relation between temperature and viscosity locks the coldest material near the planetary surface into a comparatively stiffer layer which does not participate in the active convection below it (*Davaille and Jaupart*, 1993; *Solomatov and Moresi*, 1996, 1997, 2000; *Michaut et al.*, 2025). Compared to the lithosphere of a mobile-lid planet, a thick stagnant lid can insulate the planet's interior from the surface, resulting in a different state of equilibrium or quasi-static transient state within the planet's mantle. The asymmetric inflow of heat from the core and from radiogenic sources typically drives mantle temperatures to be hotter than Earth's, which is about $1600\,\mathrm{K}$ in the present day. The planet Venus is the largest planet in our Solar System that exhibits evidence it may fall into a stagnant lid tectonic regime due to its lack of plate tectonics (*Solomatov and Moresi*, 1996).

Without plate tectonics, or a system that continuously destroys the lithosphere and subsequently replenishes it with material from the mantle, it is puzzling how such an insulated planet could have regionally high surface heat fluxes 11-116 mW/m^2, (as in *Smrekar et al.*, 2023, 2025) rivaling those of Earth (105 mW/m^2 across oceanic lithosphere, as in *Turcotte and Schubert*, 2002). It has been suggested that although Venus' lithosphere is fully connected across the planet's surface, it may be more of a 'squishy lid,' the lithosphere weakened by a high proportion of intrusive volcanism (*Lourenço et al.*, 2020; *Maia et al.*, 2025), which might lead to efficient planetary cooling. While the state of Venus' lithosphere as squishy lid or a stagnant lid (or somewhere on the continuous spectrum between the two) is still debated, this paper considers mantle dynamics and heat flow for a stagnant lid planet with no intrusive or extrusive volcanism as a lower bound, which may be regarded as a con-

*✉ mckerr@ucla.edu

servative approach. Therefore, the temporal and spatial variations in surface heat flows from numerical models of mantle convection under stagnant lid conditions more directly reflect the convective dynamics within the mantle itself, rather than intrinsic strength variations within the lithosphere.

Theoretically-derived and experimentally-verified power-law relationships between the non-dimensional convective vigor (Rayleigh number Ra), the normalized heat flux (Nusselt number Nu), and the characteristic velocity of the convecting flow in the limit of infinite Prandtl number are often used in 1D thermal evolution models or in coupled planetary-atmosphere models to understand and constrain the past evolution of many planets, based on our present-day observations (e.g., *Christensen*, 1984). Parameterized convection models are used to explore the thermal evolution of bodies in the stagnant lid regime such as icy moons, rocky moons and the inner terrestrial planets: Mars, Mercury, and Venus (e.g., *Deschamps and Sotin*, 2001; *Auerbach and Stegman*, 2025; *Michaut et al.*, 2025). Due to their ubiquitous use in planetary and Earth science problems, the empirically-determined scaling laws have been studied extensively in both numerical and analog fluid models of mantle convection. These studies span various domain geometries, modes of heating, and additional complexity such as the incorporation of depth-dependent thermophysical properties and viscosity (*Grasset and Parmentier*, 1998; *Wolstencroft et al.*, 2009; *O'Neill*, 2020; *Korenaga and Jordan*, 2003; *Garrido-Tomasini et al.*, 2025; *Reese et al.*, 1999; *Thiriet et al.*, 2019; *Grigné*, 2023; *Dubuffet et al.*, 2000). Classical boundary layer theory indicates Nu should scale with $\mathrm{Ra}^{1/3}$ and the characteristic convection velocity u_{rms} with $\mathrm{Ra}^{2/3}$ if the upper and lower thermal boundary layers of the systems are sufficiently thin and non-interacting due to the convecting interior of the mantle being well-mixed (*Turcotte and Oxburgh*, 1967). In both numerical experiments (e.g., *Moore*, 2008) and experiments using analog fluids with $\mathrm{Pr} >> 1$ (e.g., *Manga and Weeraratne*, 1999), the exponent in the power-law relation is shown to be slightly less than $1/3$ at Rayleigh numbers appropriate for mantle convection in the Earth (Ra $\sim 10^8$).

However, the appropriateness of a set of fixed universal scaling laws to explain the relationship between mantle velocity, convective vigor, and heat flow efficiency are complicated by the addition of distinct mineral phases and their transitions into the system. These phase transitions, if endothermic, can inhibit flow, affect plume dynamics, and even form two convective sub-systems within the mantle domain (*Liu et al.*, 1991; *Tackley et al.*, 1993; *Bunge, H.-P. et al.*, 1997; *Butler and Peltier*, 2000; *Wolstencroft and Davies*, 2011). If exothermic, they can rapidly increase the magnitude of thermally driven buoyancy in that region (e.g., *Faccenda and Dal Zilio*, 2017). The effects of multiple mineral phase transitions on mantle convection have been investigated for a range of parameters and to explain various geologic processes (*Liu et al.*, 1991; *Steinbach and Yuen*, 1992; *Zhao et al.*, 1992; *Peltier and Solheim*, 1992a; *Tackley et al.*, 1993; *Honda et al.*, 1993; *Solheim and Peltier*, 1994; *Yuen et al.*, 1995; *Butler and Peltier*, 2000; *Faccenda and Dal Zilio*, 2017). Mantle avalanches of cold material initiated from instabilities on an internal boundary layer within Earth (e.g., *Machetel and Weber*, 1991; *Peltier and Solheim*, 1992a; *Tackley et al.*, 1993) have been evoked to explain superchrons (long periods of stability in Earth's magnetic field) (e.g., *Weinstein*, 1993; *Eide and Torsvik*, 1996), superplume cycles (e.g., *Condie*, 1998), and perturbations in Earth's length-of-day (e.g., *Machetel and Thomassot*, 2002). As avalanches break away from the mantle transition zone, the flushing of cold material from the upper mantle induces a strong return flow which manifests as a transient spike in the surface heat flow, initiating within 10 Myrs of avalanche onset (e.g., *Solheim and Peltier*, 1994), but sometimes decaying over 100 Myr (*Yuen et al.*, 1995). These avalanches can perturb the mantle into states of disequilibrium (*Yuen et al.*, 1995) where the behaviors of the Rayleigh number, Nusselt number, characteristic velocities are not well-governed by equilibrium boundary layer theory and classic scaling relations (e.g., *Turcotte and Oxburgh*, 1967; *Jimenez and Zufiria*, 1987).

In exploring quasi-steady state convection models, where the heat flow through the boundaries remains roughly constant in time with small fluctuations at shorter timescales (SI Fig. S6-S11), we can better understand the characteristic dynamics and Ra-Nu relationship for convective regimes affected by specific sequences of mineral phase transitions relevant for the interior of Venus and other rocky planets of pyrolitic composition. This paper will demonstrate through a series of models at various mantle temperatures – and thus various sequences of realistic mineral phase transition in pyrolite – that the relationship between mantle dynamics and heat flow is more complex than a simple power law scaling relationship with an exponent of roughly $1/3$. The framework of Rayleigh-Nusselt scaling, Rayleigh-velocity scaling, and the internal energy budget will be used to showcase the complexity of planetary systems when more realistic mineral phase transitions are incorporated in compressible mantle convection models. The paper will also discuss how this complexity and non-intuitive dynamics may help explain some outstanding problems in Venus science.

First we chose appropriate and useful formulations of the Rayleigh and Nusselt numbers in mantles with layered or "leaky" phase transitions (e.g., *Christensen and Yuen*, 1985). Here, "leaky" refers to a system where there is periodic exchange of mass and heat between the two sub-regions of a layered mantle due to the build-up and release of gravitational potential energy above and below a particular endothermic phase boundary. We aim to address: does a "leaky" phase boundary in a transitional regime of partially layered convection (e.g., *Wolstencroft et al.*, 2009) inhibit or enhance the surface heat flow of the system with respect to that for a single layered convecting region? Inhibition or enhancement of heat flow could manifest either as a change in the scaling exponent β in $\mathrm{Nu}(\mathrm{Ra})$ or could manifest as a change in the constant of proportionality (a shifted power-law with the same exponent). Since scaling exponents near $\beta = 1/3$ are well established in the diverse array of literature on Rayleigh-Bérnard convection and because we do not explore baseline models without phase transitions in this study, we will not present new or different scaling exponents. Instead we will remark on the qualitative fit of the $\approx 1/3$ scaling exponent to our convecting systems whose

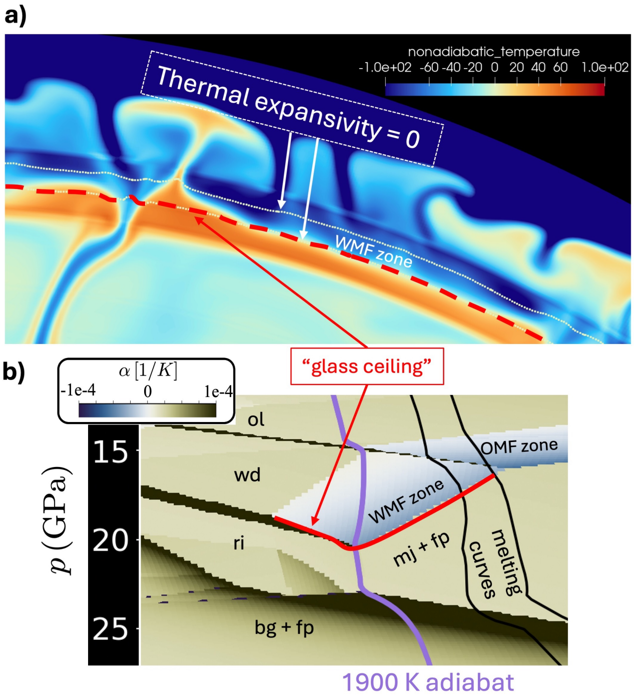

FIGURE 1 – Annotated section of the upper-most part of the mantle domain with potential temperature $\approx 1900\,\mathrm{K}$ with contours of 0 coefficient of thermal expansivity [1/K] (a) and a sketch of the stable phases in the upper mantle for anhydrous pyrolite with the 1900 K adiabat in purple (b). The "glass ceiling" (highlighted in red in (b)) is the lower-pressure boundary of the broad endothermic phase transition of wd = mj + fp where both hot and cold material layers, as in the stagnant lid models discussed in this paper and in *Kerr et al.* (2025). It has both positive and negative "slope" in p-T space but in its entirety represents an endothermic (i.e., negative Clapeyron slope) phase transition.

dynamics are dominated by the effects of mineral phase transitions.

It is possible Venus manifests the effects of a particular and unusual phase transition. Based on interpretation of radar images, gravity, and topography data, Venus has roughly the same number ($\sim$9) of large mantle plumes (*Smrekar and Sotin*, 2012) as Earth might have (*Courtillot et al.*, 2003), all of which are inferred to originate at the core-mantle boundary. Unlike Earth, Venus also has 740 coronae, quasi-circular volcano-tectonic features ranging in diameter from 60-1000 km (a mean value of ~ 200 km) typically attributed to small scale plumes (*Stofan et al.*, 1991; *Koch*, 1994; *Gülcher et al.*, 2025). The origin of these small-scale features has been debated. Previous work by this group, *Kerr et al.* (2025), postulates that the seemingly paradoxical coexistence of large volcanic rises and coronae on Venus might be explained by a convective regime defined by the broad endothermic mineral phase transition of wadsleyite to majorite plus ferropericlase (WMF transition) which induces layering of both cold and hot convective features within the mantle transition zone between 500 and 700 km depth (Figure 1). We call this regime the "glass ceiling" which is the shorthand for the higher pressure boundary of the WMF transition zone. Specifically, the hot return flow from the lower mantle into the upper mantle induced by the mantle avalanches is not dictated by boundary layer scaling in this interior transition due to the "leaky" behavior of the transition. The WMF transition can therefore produce a wide size range and number of concurrent hot upwellings that may not be well-governed by boundary layer theory.

The WMF transition in an equilibrium pyrolite composition, for mantle potential temperatures above $1700\,\mathrm{K}$, has been characterized by mineral physics experiments and thermodynamic modeling (*Stixrude and Lithgow-Bertelloni*, 2005a, 2011, 2021) and determined to have a strongly negative phase buoyancy and negative Clapeyron slope which may have important effects on convection in the early Earth (*Dannberg et al.*, 2022; *Li et al.*, 2025) and in present-day Venus (*Kerr and Stegman*, 2024; *Kerr et al.*, 2025). This transition is broad and is bounded from above by the exothermic reaction of wadsleyite to olivine under decreasing pressure conditions and bounded from below by the transition of wadsleyite to ringwoodite (exothermic for adiabats cooler than $1900\,\mathrm{K}$) and then to bridgmanite around 25 GPa. Starting along the $1700\,\mathrm{K}$ adiabat and increasing in temperature from there, at 18 GPa some of the wadsleyite phase transforms into majorite and ferropericlase (denser phases). This transition from a less dense phase to a denser phase under the conditions of increasing temperature gives it an effective negative coefficient of thermal expansivity α (*Stixrude and Lithgow-Bertelloni*, 2021; *Dannberg et al.*, 2022). In this study, we investigate the peculiarities of heat flow in models within the "glass-ceiling" convective regime, describe first-order qualities for the scaling relationships between convective vigor (Ra) and heat flow (Nu), and connect these results to outstanding problems in Venus research.

2 Summary of numerical modeling methods

We present a summary of both the purely bottom-heated and purely internally-heated mantle convection models used to examine heat flow and scaling trends in the "glass-ceiling" convective regime. The suite of basally-heated models presented in this study are similar to those in *Kerr and Stegman* (2024) and *Kerr et al.* (2025). We model Venus' convecting mantle as a compressible fluid (ignoring bulk viscosity) in 2D cylindrical annulus geometry with the geodynamic code ASPECT to solve the governing equations of mass, momentum, and energy (*Kronbichler et al.*, 2012; *Heister et al.*, 2017; *Bangerth et al.*, 2022). The simulations are formulated to use the projected density approximation for the mass conservation law (*Gassmöller et al.*, 2020) and an entropy formulation of the energy equation (*Dannberg et al.*, 2022). The equations are:

$$-\nabla \cdot (2\eta\dot{\varepsilon}) + \nabla p = \rho_h \mathbf{g} \tag{1}$$

$$\frac{\partial \rho_h}{\partial t} + \mathbf{u} \cdot \nabla \rho_h + \rho_h \nabla \cdot \mathbf{u} = 0 \tag{2}$$

$$\rho_h T \left(\frac{\partial S}{\partial t} + \mathbf{u} \cdot \nabla S \right) + \rho_h C_p \left. \frac{\partial T}{\partial t} \right|_{\mathrm{cond}} = 2\eta\dot{\varepsilon} : \dot{\varepsilon} + \rho_h H_{\mathrm{r}} \tag{3}$$

where η is viscosity, $\dot{\varepsilon}$ is the deviatoric strain-rate, p is pressure, $\mathbf{g}$ is the gravitational acceleration of Venus ($8.87\,\mathrm{m\,s^{-2}}$), ρ_h is the density derived from the hydrostatic pressure (*Gassmöller et al.*, 2020), $\mathbf{u}$ is the velocity vector, t is time, T is temperature, S is specific entropy, and C_p is the specific heat capacity at constant pressure. H_r is the radiogenic component of internal heating in $\mathrm{W/kg}$ and pertains only to the purely internally-heated models. The mesh of the model consists of quadrilateral finite elements (Q2 elements for velocity, Q1 elements for pressure) with a resolution of 128×1536 cells, equivalent to about 23 km grid spacing at the surface. Summary of fixed models parameters can be found in Table 1 and varied parameters in Table 2. The viscosity is Newtonian and temperature- and depth-dependent, composed of an Arrhenius-type reference viscosity that varies only with depth and a multiplicative lateral-variation term (e.g., *Steinberger and Calderwood*, 2006) that depends on both depth and temperature. The equations are:

$$\eta_{\mathrm{ref}}(r) = A \exp\left[\frac{E + p(r)\,V_{\mathrm{act}}}{nR\,T_{A,0}(r)}\right] \tag{4}$$

$$\eta(T,r) = \eta_{\mathrm{ref}}(r)\,\eta_{\mathrm{lat}}(r,T) \tag{5}$$

$$\eta(T,r) = A \exp\left[\frac{E + p_0(r)\,V_{\mathrm{act}}}{nR\,T_{A,0}(r)}\right] \times \exp\left[\frac{-H_{\mathrm{lat}}\,(T - T_{A,0}(r))}{nR\,T\,T_{A,0}(r)}\right] \tag{6}$$

where E is the activation energy, V_{act} is the activation volume, $p_0(r)$ is the initial adiabatic pressure profile through the mantle, $T_{(A,0)}(r)$ is the initial adiabatic temperature profile, H_{lat} is the activation enthalpy for lateral variations in viscosity due to temperature, $n = 1$ for pure diffusion creep, and R is the gas constant $8.314\ \mathrm{J\,mol^{-1}\,K^{-1}}$. The activation enthalpy H_{lat} is a constant value in each model, owing to the separation of the temperature and depth dependencies of viscosity, and is given by $E + 2.3 \times 10^{10}\ V_{\mathrm{act}}$ where 2.3×10^{10} Pa is the pressure at the base of the mantle transition zone. The activation energy E is 240 kJ/mol, and the activation volume is given in Table 2 and varied to generate the desired reference viscosity contrast across the domain. The scaling coefficient A is defined such that along the initial adiabat at the surface ($p = 0$) and at a temperature of $1600\ \mathrm{K}$, the viscosity is $\eta = 10^{21}\ \mathrm{Pa \cdot s}$.

To define the equation of state, our models use a thermodynamic look-up table for pyrolite which is supplied with pressure p and specific entropy S as independent variables. Therefore, the density ρ, temperature T, and specific heat C_p are updated throughout the model evolution and projected onto the mesh where solution variables, such as S, are computed and defined at each timestep (*Gassmöller et al.*, 2020). This look-up table is generated by the thermodynamics software HeFESTo (*Stixrude and Lithgow-Bertelloni*, 2005b, 2011, 2021) which inverts mineral physics experimental data and uses a Gibbs Free Energy minimization scheme to map out the equilibrium mineral phases for a given bulk composition across the p and S space of terrestrial mantles. We do not consider the role of mineral phase transition reaction kinetics, which have been shown (e.g., *King et al.*, 2015) to affect downwelling behavior by allowing for the metastability of minerals in the thick down-going slabs characteristic of mobile-lid planetary convection. Additionally, we neglect the effects of dynamic pressure on the density field ρ_h in the governing equations which introduces some errors into the flow of mechanical energy and the depths of phase transitions in the modeled mantle. These errors are small and described in Supplementary Information, Appendix I.

Our models employ a single component multiphase assemblage with the composition of pyrolite as defined in *Xu et al.* (2008) and used in *Dannberg et al.* (2022), *Li et al.* (2025), and in *Kerr and Stegman* (2024) and *Kerr et al.* (2025) by this group. A more complex system with multiple components, and therefore multiple sets of stable phases, would be a more realistic system as melt differentiates a chemically equilibrated composition like pyrolite into a mechanical mixture of enriched and depleted partial melt end-members. However, as found by *Kerr and Stegman* (2024), and *Kerr et al.* (2025), even a single component's mineral phase transitions can generate complex and unintuitive dynamics with regards to mantle layering when employed in 2D whole mantle convection simulations.

Our model suite consists of thirteen bottom-heated and five internally heated mantle convection simulations that primarily vary in their effective thermal forcing from the core and in their initial mantle potential temperatures. A summary of the initial and boundary conditions for our model is described in Figure 2a along with initial temperature profiles (Figure 2b) passing through the phase space of pyrolite, colored in the background by the density of the material. Melting curves for anhydrous pyrolite are provided for reference and are not incorporated in any calculations. Figure 3a shows the coefficient of thermal expansivity field and the mean temperature profiles for eight bottom-heated model evolutions overlaid. Since the simulations use entropy instead of temperature in the governing equation for energy conservation, the boundary conditions and initial conditions are presented in terms of the specific entropy S which we will discuss in terms of potential temperature (i.e., the temperature for a material at that specific entropy S at a pressure of $p = 0$, the surface of the planet). For a surface temperature of $740\ \mathrm{K}$ which is typically assumed for Venus, the pressure is $0\ \mathrm{GPa}$ and the specific entropy is $1602.8\ \mathrm{J\,K^{-1}\,kg^{-1}}$. The core temperature for each model remains constant throughout its evolution and is defined by an entropy corresponding to a $600\ \mathrm{K}$ increase from the real temperature along the initial adiabat at the base of the mantle.

The effective thermal forcing from the core is additionally controlled by the radial dependence of the reference mantle viscosity $\eta_{\mathrm{ref}}(r)$. We define a parameter $\Delta\eta_{\mathrm{ref}}$ as the ratio between the reference viscosity at $p = 0\ \mathrm{GPa}$ (depth $z = 0$) and the reference viscosity at $p = 119\ \mathrm{GPa}$ ($z = 2942\ \mathrm{km}$ depth) which is roughly the base of the mantle depending on the initial mantle temperature and its associated density profile. We explore two values of $\Delta\eta_{\mathrm{ref}}$: 30 and 100, representing a weak and moderate increase of viscosity, respectively. An increase of $\Delta\eta_{\mathrm{ref}}$ represents an increase in viscosity with depth and dynamically manifests a concentration of thermal upwellings into fewer, larger mantle plumes. A higher reference viscosity ratio also reduces the overall heat flow from the lowermost mantle to the mid-mantle region, as it is harder to move material in the lower mantle through plume conduits and laterally along the core-mantle boundary for higher values of $\Delta\eta_{\mathrm{ref}}$. This increasing viscosity corresponds to lowering the effective Rayleigh number as they are inversely proportional. For $\Delta\eta_{\mathrm{ref}} = 30$ and 100, we run simulations of bottom-heated stagnant lid mantle convection (i.e., no yielding of the lithosphere) with initial mantle potential temperatures $T_{\mathrm{pot},0} = T_{A,0}(z = 0)$ of $1600\ \mathrm{K}$, $1700\ \mathrm{K}$, $1800\ \mathrm{K}$, $1900\ \mathrm{K}$, and $2000\ \mathrm{K}$. For $\Delta\eta_{\mathrm{ref}} = 100$, we run three additional simulations with mantle temperatures of $1860\ \mathrm{K}$, $1950\ \mathrm{K}$, and $2050\ \mathrm{K}$ to add coverage to the particular region of phase space of interest, the region where the WMF zone has the greatest dynamical effect. We also add five internally heated models with $\Delta\eta_{\mathrm{ref}} = 100$ to confirm the results are valid in the other end-member mode of heating. The set of mantle temperatures explored in these models is chosen to span the dynamics of solid-state convection from Earth-like potential temperatures ($1600\ \mathrm{K}$) up to the melting curves. Although the $2000\ \mathrm{K}$ and hotter models would experience significant melting were it accounted for, we run these models to observe changes in heat flow solely due to solid-state convective effects.

We note that the pyrolite equation of state defined by the HeFESTo table will be continuously updated and improved with additional mineral physics experiments and theoretical calculations in the future. Additionally, beyond potential temperatures of approximately $1950\ \mathrm{K}$ it becomes increasingly unrealistic to model the planet as purely solid-state convection without melt generation, transport, extraction, or the effect of the partially melted phase on the physical properties of the silicate. In this light, our paper is meant to highlight that as mantle convection models become more complex and incorporate more detailed, self-consistent physics, the underlying distinct mechanisms of heat transfer and internal thermal evolution may become more difficult to distinguish. By neglecting melting for now, we can gain an understanding of how multiple endothermic and exothermic mineral phase transitions can affect solid-state convection and use this understanding as a baseline before adding melting physics, multiple components, and other more detailed planetary processes. Further information about the numerical methods and model set-up can be found in *Stixrude and Lithgow-Bertelloni* (2005a, 2011); *Gassmöller et al.* (2020); *Dannberg et al.* (2022); *Stixrude and Lithgow-Bertelloni* (2021); *Kerr and Stegman* (2024); and *Kerr et al.* (2025).

3 Rayleigh-Nusselt scaling for stagnant lid convection

The intuitive effect of endothermic phase transitions is to reduce mass flux through that boundary (e.g., *Richter and McKenzie*, 1981; *Olson and Yuen*, 1982; *Peltier and Solheim*, 1992a,b; *Tackley et al.*, 1993), even to layer the material entirely along the transition, thereby reducing the efficiency of heat flow (i.e., Nu) through the system. An associated reduction in surface heat flux has been observed in numerical models of convection that have explored systematic increases in the magnitude of the negative Clapeyron slope ($\gamma = dP/dT$) of an endothermic phase transition (*Butler and Peltier*, 2000; *Wolstencroft and Davies*, 2011; *Herein et al.*, 2013). Additional research on more complex systems such as an endothermic transition at ~ 660 km depth and an exothermic ($dP/dT > 0$) transition at ~ 410 km depth, for an Earth-like mantle, implied that the addition of the exothermic transition increased the propensity of the convecting material to layer, further reducing the heat flow efficiency through the system (*Steinbach and Yuen*, 1992). In mantle silicates, the arrangement of stable phases is more complex (e.g., *Stixrude and Lithgow-Bertelloni*, 2021) than one- or two-phase transitions represented by a fixed thickness and/or a constant Clapeyron slope throughout the entire temperature range of the mantle transition zone. We explore Ra-Nu relationships in the context of these more complex mantles, before introducing other realistic physics in future work such as melting, which we understand to be an important thermal and dynamic influence on planetary evolution, particularly for Venus.

The first step is to motivate a choice for the formulation of the nondimensional convective vigor (Ra) and normalized heat flow (Nu). The classical definition for the Rayleigh number of a convective system is:

$$\mathrm{Ra} = \rho g \alpha\, \Delta T\, D^3/(\kappa \eta_i) \tag{7}$$

where η_i represents the viscosity associated with T_i, the well-mixed interior temperature of the system. This formulation is applicable to mantle convection models employing a Boussinesq approximation where compressibility is neglected and the temperature profile through the entire well-mixed interior is represented by the mantle potential temperature. In compressible systems with adiabatic temperature increasing with depth, as well as depth-dependent thermodynamic properties and viscosities in the mantle, such a formulation can become complicated. Due to the layering effects of the WMF, in this study we define the Rayleigh number with the volumetrically averaged values of the thermo-physical properties in each well-mixed interior. For an examination of layered convection, there are two mixing "interiors" to consider: (1) the lower mantle from below the mantle transition zone (MTZ) to the core, 30–119 GPa on Venus; and (2) the upper mantle from the MTZ up to the base of the lithosphere, X–15 GPa, where X is a placeholder for the pressure at the base of the lithosphere, changing for each model, as the steady-state lithosphere thickness for each model is different.

To avoid boundary layer effects and the horizontal deflection of radial velocities near the MTZ, we define our "well-mixed interiors" as 50–90 GPa for the lower mantle (LM) and 10–15 GPa for the upper mantle (UM). For the coldest models with the thickest lithosphere, 10 GPa is still too shallow; however, we apply the 10–15 GPa definition of the upper mantle to all models and contextualize these results for the coldest models, removing the coldest models with the thickest lithosphere in our analysis. These regions are visualized for the 1800K-100x model in Figure 3b. We define:

$$\mathrm{Ra}_1 = \bar{\rho}_{\mathrm{LM}}\, g\, \bar{\alpha}_{\mathrm{LM}}\, (T_{\mathrm{pot,LM}} - T_s)\, D^3/(\bar{\kappa}_{\mathrm{LM}} \bar{\eta}_{\mathrm{LM}}) \tag{8}$$

and

$$\mathrm{Ra}_2 = \bar{\rho}_{\mathrm{UM}}\, g\, \bar{\alpha}_{\mathrm{UM}}\, (T_{\mathrm{pot,UM}} - T_s)\, d_{\mathrm{MTZ}}^3/(\bar{\kappa}_{\mathrm{UM}} \bar{\eta}_{\mathrm{UM}}). \tag{9}$$

The symbol d_{MTZ} represents the depth of the mantle transition zone which we approximate as 600 km throughout the

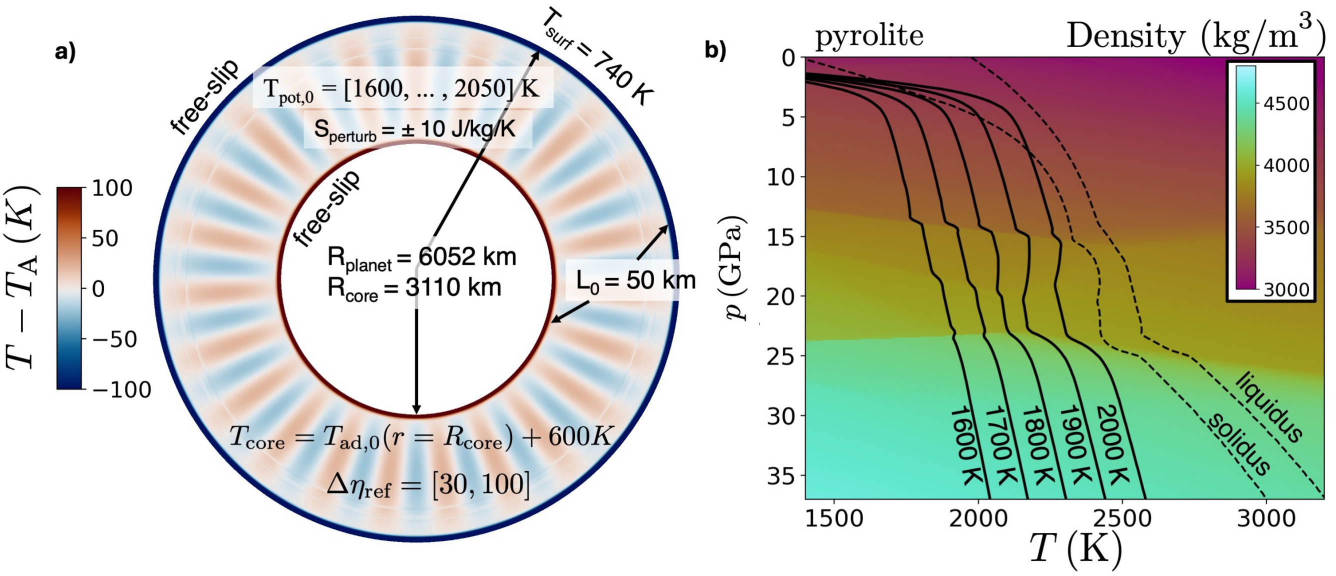

FIGURE 2 – (a) A summary of model initial conditions, boundary conditions, and model geometry. The initial cold and hot thermal boundary layers are $50\,\mathrm{km}$ thick at $t = 0$. A $10\,\mathrm{J\,kg^{-1}\,K^{-1}}$ specific entropy perturbation with azimuthal wavelength $\ell = 23$ is imposed to drive short-wavelength convection, which then damps to a longer-wavelength structure as the system approaches steady state. **(b)** Initial mantle temperature profiles for the $1600\,\mathrm{K}$, $1700\,\mathrm{K}$, $1800\,\mathrm{K}$, $1900\,\mathrm{K}$, and $2000\,\mathrm{K}$ models overlaid on a density color-map for pyrolite in the upper mantle region. Melting curves for anhydrous pyrolite (*Stixrude et al.* (2009)) are the dashed black lines, which indicate at the higher temperatures, the influence of melting on dynamics and surface heat flow becomes increasingly important, though not explored in this paper (but discussed in Supplementary Information for *Kerr et al.* (2025)).

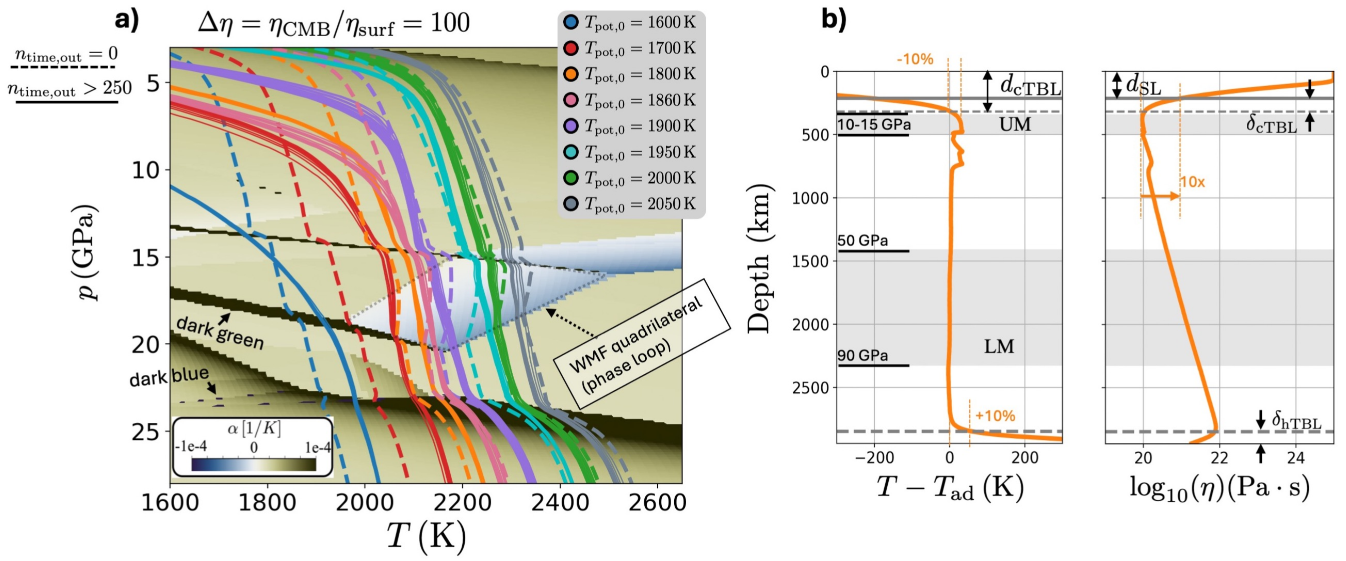

FIGURE 3 – (a) A colormap of the coefficient of thermal expansivity for a pyrolite composition in the temperature and pressure range for Earth's and Venus' upper mantles. The central light blue parallelogram (WMF quadrilateral) is the broad transition region from wadsleyite to majoritic garnet and ferropericlase. Overlaid are temperature profile evolutions for eight models: $1600\,\mathrm{K}$ (blue), $1700\,\mathrm{K}$ (red), $1800\,\mathrm{K}$ (orange), $1860\,\mathrm{K}$ (pink), $1900\,\mathrm{K}$ (purple), $1950\,\mathrm{K}$ (cyan), $2000\,\mathrm{K}$ (green), and $2050\,\mathrm{K}$ (gray). The profiles at the initial (dashed) and post-transient (solid) times are displayed. **(b)** An example pair of non-adiabatic temperature and viscosity profiles showing the pressure range for the upper and lower "well-mixed" mantle regions for the 1800K-100x model. d_{cTBL} is the depth at the base of the cold thermal boundary layer; d_{SL} is the depth and thickness of the stagnant lid (10$\times$ the viscosity of the upper mantle); and δ_{hTBL} and δ_{cTBL} are the hot and cold thermal boundary layer thicknesses, respectively.

entire analysis. In both formulations of the Rayleigh number, we use a ΔT representing the temperature contrast available for convection, ignoring the adiabatic increase in temperature with depth. For Ra_1 this means that the maximum temperature we use is the potential temperature associated with the well-mixed interior, $T_{\mathrm{pot,LM}}$. For Ra_2, we use the potential temperature associated with the mean upper mantle entropy between 10 and 15 GPa, $T_{\mathrm{pot,UM}}$.

We also define the surface Nusselt number, which we simply call the Nusselt number throughout the manuscript, as the heat flow efficiency of the whole mantle system. Since our models are two-dimensional, the surface area of the core-mantle boundary with respect to the surface area of the mantle-atmosphere boundary is overestimated, lead-

Variable	Symbol	Value
Velocity	$\mathbf{u}$	model solution [m/s]
Temperature	T	from HeFESTo [K]
Specific Entropy	S	model solution [J/K/kg]
Pressure	p	model solution [Pa]
Thermal expansivity	α	from HeFESTo [1/K]
Specific heat capacity	C_p	from HeFESTo [J/kg/K]
Viscosity	η	computed as reference profile [Pa·s]
Gravity	g	8.87 [m/s^2]
Thermal conductivity	k	4.7 [W/m/K]
Density	ρ	from HeFESTo [kg/m^3]
Strain rate	$\dot{\varepsilon}$	derived from model solution $\mathbf{u}$: $\dot{\varepsilon} = \frac{1}{2}(\nabla\mathbf{u} + (\nabla\mathbf{u})^T)$[1/s]
Surface temperature	T_{surf}	740 [K]
Planetary radius	R_p	6052 [km]
Core radius	R_c	3110 [km]
Depth of domain	D	2942 [km]

TABLE 1 – Variables in thermal convection equations and their values.

Model name	T_{core} [K]	$S_{m,0}$ [J/kg/K]	S_{core} [J/kg/K]	V_{act} [m^3/mol]	$\Delta T_{\text{CMB},0}$ [K]	H_r [W/kg]
1600K-30x	3177.97	2535.079	2802.615	1.92e-6	602	0
1600K-100x	3177.97	2535.079	2802.615	2.05e-6	602	0
1700K-30x	3322.09	2612.901	2858.348	1.86e-6	599	0
1700K-100x	3322.09	2612.901	2858.348	2.09e-6	599	0
1800K-30x	3486.90	2687.720	2920.014	1.92e-6	596	0
1800K-100x	3486.90	2687.720	2920.014	2.16e-6	596	0
1860K-100x	3486.90	2731.520	2920.014	2.16e-6	492	0
1900K-30x	3656.08	2760.360	2980.340	1.98e-6	593	0
1900K-100x	3656.08	2760.360	2980.340	2.24e-6	593	0
1950K-100x	3752.45	2796.140	3013.283	2.28e-6	600	0
2000K-30x	3830.53	2831.620	3039.992	2.05e-6	589	0
2000K-100x	3830.53	2831.620	3039.992	2.32e-6	589	0
2050K-100x	3934.03	2866.710	3073.892	2.37e-6	601	0
1600K-100x-int	–	2535.079	–	2.05e-6	–	1.31e-12
1700K-100x-int	–	2612.901	–	2.09e-6	–	1.43e-12
1800K-100x-int	–	2687.720	–	2.16e-6	–	2.11e-12
1900K-100x-int	–	2760.360	–	2.24e-6	–	3.18e-12
2000K-100x-int	–	2831.620	–	2.32e-6	–	4.92e-12

TABLE 2 – A summary of the varied parameters for the numerical models discussed in this paper. T_{core} is the temperature of the core, $S_{m,0}$ is the initial mantle specific entropy, S_{core} is the fixed specific entropy of the core, V_{act} is the activation volume, $\Delta T_{\text{CMB},0}$ is the initial temperature contrast across the CMB, and H_r is the constant radiogenic heating rate. Additional information about the model set-up and fixed parameters can be found in *Kerr et al.* (2025) and Appendix B in the Supplemental materials.

ing to higher core heat flows into the domain which may translate into higher mantle temperatures or a different energetic balance within the system (*Fleury et al.*, 2024, Supp. Appendix C). This can have complicated effects for long thermal-evolution models, which is why we focus on 2D cylindrical models that stay near or approach a fixed mantle temperature in order to understand the dynamics for these more stable systems where the ambient mantle temperature determines the main stable phases in the mantle and thus the dynamics. We also are careful to use a conductive solution in the Nusselt number that is specifically scaled for 2D infinite cylinder geometry, as described below.

For a 2D cylindrical geometry, the domain acts as an infinitely long cylinder with an inner radius equivalent to Venus' approximate core radius of 3110 km and the outer radius as Venus' planetary radius, or surface radius: 6052 km. The purely conductive heat flow density (i.e., the 2D model equivalent of heat flow which is described in Watts per unit length along the infinite cylinder) that travels radially through a cylinder with a constant hot interior boundary and a constant cold exterior boundary is given by:

$$Q_{\text{cond}} = 2\pi k(T_{\text{cmb,mantle}} - T_{\text{surf}})/\ln\left[\frac{R_p}{R_c}\right]. \qquad (10)$$

where $T_{\text{cmb,mantle}}$ is the azimuthally averaged temperature just above the basal boundary, at the resolution of the depth average output file of the model (roughly 5 km) which was set to have 500 interpolated, evenly-spaced points along the 2942 km depth profile. This definition for $T_{\text{cmb,mantle}}$ is chosen such that the temperature contrast across the domain can be computed consistently for both basally heated and internally heated models. This is similar to how *Reese et al.* (2005) define the conductive reference in their Nusselt number for their purely internally heated models, based on the mantle internal temperature. Here, the true temperature just above the core-mantle boundary is taken to approximate the maximum azimuthally-averaged temperature in the domain for both basally-heated and internally-heated models. Since internally heated models have approximately uniform internal heating, and the viscosity at depth is large, resisting convective flow away from the base of the mantle, the temperature near the insulated boundary is characteristic of the interior temperature of the domain and a suitable choice for computing the temperature contrast across the system. For basal heating, this choice is also appropriate since the sampled depth is well within the hot thermal boundary layer above the core and within $100\,\mathrm{K}$ of core temperature at $5\,\mathrm{km}$ above the CMB. We can also use the potential temperature of the lower mantle region $T_{\mathrm{pot,LM}}$ as the interior temperature in our computation of the Nusselt number for both heating modes, which does not have an influence on our primary results (see Supplemental Information, Appendix G).

We can extract the total surface heat flow density of our models conducted through the lithosphere by interpolating the temperature field in the finite element mesh along a contour of shallow enough constant radius which we choose as an arbitrarily shallow depth of 10 km below the surface. Since ASPECT solves equations 1,2, and 3 in Cartesian coordinates, regardless of the domain geometry, we use the Python package PyVista (*Sullivan and Kaszynski*, 2019) to convert the system into a polar coordinate system and use contours of constant radius to extract the temperature at arbitrary choices of fixed depth within the conductive lithosphere. The Q2 element resolution near the surface is 23 km, so the values at a depth of 10 km are interpolated. We extract the surface heat flux which can be integrated over the circumference of the cylindrical exterior:

$$Q_{\mathrm{surf}} = 2\pi R_p \bar{q}_{\mathrm{surf}} \tag{11}$$

where $\bar{q}_{\mathrm{surf}}$ is the mean surface heat flux computed from the temperature field contour using Fourier's law of conduction. The Nusselt number is the ratio of total heat flow through the system over the heat flow through the system where the interior is purely conductive. We express:

$$\mathrm{Nu} = Q_{\mathrm{surf}}/Q_{\mathrm{cond}} = \frac{\bar{q}_{\mathrm{surf}} R_p \ln\left[\frac{R_p}{R_c}\right]}{k(T_{\mathrm{cmb,mantle}} - T_{\mathrm{surf}})}. \tag{12}$$

Because we defined the conductive reference heat flow Q_{cond} to be agnostic to the mode of heating in the system, the Nusselt number we compute is formulated the same way for all models. We discuss this rationale below.

For models in which there are large downwellings (mantle avalanches) that bring cold material to the lower mantle, both the depth-dependence of viscosity as well as the choice of depth to measure $T_{\mathrm{cmb,mantle}}$ ensure that Q_{cond} is not downwardly biased by these downwellings. One may argue we should also define both the internally-heated and basally-heated models in terms of their flux Rayleigh numbers and Nusselt numbers, as discussed in the Supplemental Information (Appendix D). However, as we will discuss later (Discussion section 5.3), there is a purpose to having these dimensionless convective parameters formulated for all models either completely in terms of temperature contrasts across the domain or in terms of energy flow, regardless of the heating mode. In short, we formulate solely in terms of temperature contrast due to the sensitive energetics of our inclusion of compressibility effects and multiple endothermic and exothermic mineral phase transitions in these models.

The classic Rayleigh-Nusselt relationship (*Priestley*, 1954; *Malkus*, 1954) is a power law, given by:

$$\mathrm{Nu} = a\mathrm{Ra}^{\beta}. \tag{13}$$

The value of the exponent β is the matter of some debate. In *Turcotte and Oxburgh* (1967), β was shown to be $1/3$ using boundary layer theory for isoviscous convection in a unit square box. For mantle convection models with a stagnant lid and using the same scaling law as Equation (13), several studies indicated that the value of β could be as low as 0.1 in stagnant lid convection (*Christensen*, 1984) up to the theoretical value of $1/3$ with several numerical and physical experiments finding intermediate values of β (*Hansen and Ebel*, 1984; *Olson*, 1987; *Bercovici et al.*, 1989; *Gurnis*, 1989; *Giannandrea and Christensen*, 1993; *Ratcliff et al.*, 1996; *Iwase and Honda*, 1997; *Korenaga and Jordan*, 2003; *Wolstencroft et al.*, 2009; *O'Neill*, 2020). Table 4 in the paper *Wolstencroft et al.* (2009) has a summary of these previously calculated and measured scaling relationships. Further insight by *Solomatov* (1995) and *Davaille and Jaupart* (1993) argued that the classic Ra–Nu relation should be augmented when the viscosity of the convecting fluid depends on temperature exponentially and the system forms a stagnant lid on the uppermost boundary which does not participate in the convection below. In their formulations, they include the Frank-Kamenetskii parameter θ (*Frank-Kamenetskii*, 2015), arguably first used in the context of mantle viscosity in *Solomatov and Moresi* (1996), which describes the strength of the temperature dependence of viscosity, and thus the propensity for the system to have a *stagnant* lid due to the viscosity contrast between the surface and interior temperature conditions (*Davaille and Jaupart*, 1993; *Solomatov*, 1995; *Solomatov and Moresi*, 2000). This updated formulation of Equation 13 is:

$$\mathrm{Nu} = a\theta^{-(1+\beta)}\mathrm{Ra}^{\beta}, \tag{14}$$

or equivalently

$$\mathrm{Nu}\theta = a\frac{\mathrm{Ra}^{\beta}}{\theta}, \tag{15}$$

where $\beta = 1/3$ remains the theoretical asymptotic scaling exponent where θ is incorporated into the scaling law (*Solomatov*, 1995). The viscosity laws in our models are both depth and temperature dependent, so we take $\theta = \ln\Delta\eta \approx \ln\left(-\frac{d\eta}{dT}\Delta T\right)$, where ΔT is the non-adiabatic temperature jump from the interior to the surface and $d\eta/dT$ is evaluated at the surface using the viscosity law for each model (Equation (6)). We represent ΔT in the same way that we represent it in Ra_1, as $\Delta T = T_{\mathrm{pot,LM}} - T_s$, ignoring the adiabatic increase of temperature with depth through the domain in order to consider only the change in temperature that is available for convection. We define:

$$\Delta\eta = \frac{\eta(z=0, T=T_s)}{\eta(z=0, T=T_{\mathrm{pot,LM}})} = \frac{H_{\mathrm{lat}}(T_{\mathrm{pot,LM}} - T_s)}{T_{\mathrm{pot,LM}} \cdot T_s}. \tag{16}$$

We can also approximate θ using $T_{\mathrm{pot,UM}}$ instead of $T_{\mathrm{pot,LM}}$ which does not affect our primary results (Supplemental Information: Appendix G).

In the next section, we will outline salient features and dynamics of the model suite and analyze them through the framework of Rayleigh–Nusselt scaling. For each of the models, we examine the time series of the Rayleigh number and Nusselt number for all timesteps after the initial transient stage of the model. The removal of this transient stage encompassed by the first 250 timesteps of each model's evolution ensures that we are computing our Ra–Nu scaling laws when the model is exhibiting steady, but not necessarily non-zero, heat flow into and out of the system (Supplementary Information, Appendix E, Figs. S6–S11). These 250 timesteps encompass the maximum amount of "burn-in" time that the model undergoes from the initial perturbation of 23 upwellings and downwellings to a state of longer wavelength convection as these initial plumes merge into a more stable configuration. This state of steady heat flow is distinct from "steady-state," which would imply that the thermodynamic state variables (i.e., temperature, entropy) are not varying with time. Our temperatures drift steadily over time due to the steady, but net positive or negative heat flow through the system.

We describe our models to be in a quasi-steady state after all the initial plumes have merged to a lower order configuration of convection and when the surface heat flow evens out or the mantle temperature changes linearly in time at a low rate. This rate ranges from 0–$30\,K/\mathrm{Gyr}$ for this suite of models, while the average rate of temperature change $\approx 5\,K/\mathrm{Gyr}$. Due to the compressibility and phase transitions in the system, heat flow into and out of the system is rarely completely steady, even after many overturns. However, we can apply steady state scaling laws to models undergoing transient cooling or heating since (1) the heating and cooling after the merging transient stage is quite low (only a couple degrees K over 100 Myrs, on average), and (2) these transient states (each time-step) can be treated as successive equilibria where the mean Rayleigh and Nusselt numbers are appropriate diagnostics of its state at that time (e.g., *Daly*, 1980). This can be seen in particular for the 1700 K models that undergo long secular heating trends; using the relevant upper mantle Ra throughout the model evolution (which defines the state of the mantle directly below the conductive lithosphere), the exponent β' trends near $1/3$ (Fig. 9b).

4 Results

The primary result we report is a change in the coefficient of the Ra–Nu power-law relationship between pyrolitic models with temperatures of 1600 K to 1900 K and from 1950 to 2050 K. A summary of some thermal and dynamic characteristics of our 18 models are given in Table 4, 5, 6, and 7. The volumetric average of specific entropies in the upper mantle and lower mantle are converted into potential temperatures (following an adiabatic temperature profile to the surface). We note for the models with the coldest average mantle temperatures (e.g., $1600\,\mathrm{K}$-$100\times$, Table 2), the base of the lithosphere extends down to 10 GPa, and the lithosphere's much lower temperature downwardly biases the averaged thermo-physical properties used in Ra_2. In such cases where the upper mantle is examined, the $1600\,\mathrm{K}$-$100\times$ model is taken as an outlier.

Temperature profiles over the pressure range of the mantle transition zone are shown in Figure 3 for all eight of the bottom-heated models with the fixed parameter $\Delta\eta_{\mathrm{ref}} = 100$. Each of these eight models plotted here pass through distinct regions of phase space where the effective thermal expansivity varies along the profile due to the different exothermic and endothermic transitions. For example the $1600\,\mathrm{K}$ model, at its final timestep, passes through the olivine to Wadsleyite transition (not shown) and from wadsleyite to ringwoodite at 18 GPa. The temperature profile then passes across the endothermic ringwoodite to bridgmanite transition around 23 GPa. The $1800\,\mathrm{K}$ model passes through the wadsleyite to ringwoodite transition (exothermic) at around 20 GPa, but the mean profile of the $1900\,\mathrm{K}$ model does not pass through a stable phase of ringwoodite and instead passes through the WMF zone directly into the garnet + ferropericlase phase before transforming to bridgmanite at 23 GPa. The depths and thermophysical properties of the phase transitions vary depending on the mantle's mean specific entropies, and these varying factors affect the convective dynamics and energy flow in the system.

For each timestep of each model, the thickness of the stagnant lid and the thicknesses of the actively convecting region of the cold and hot thermal boundary layers are also measured. The stagnant lid thickness is defined, as shown in Figure 3b, as the depth for which the azimuthally averaged mantle viscosity is 10 times that of the minimum azimuthally averaged viscosity in the upper mantle (e.g., *Jellinek and Lenardic*, 2009). Stagnant lid thickness has also been defined by *Davaille and Jaupart* (1993) according to the inflection point of the $v_z T$ curve through the mantle. We compute the stagnant lid both ways but note that they do not differ by more than 10% from each other (mostly within 5%), and the former $10\times$ method is resolved more smoothly through the initial transient stage of our models (see Supplemental Information, Figure S4).

The time evolution of the non-adiabatic temperature field with depth for the $1600\,\mathrm{K}$, $1700\,\mathrm{K}$, $1800\,\mathrm{K}$, $1900\,\mathrm{K}$ and $2000\,\mathrm{K}$ models with $\Delta\eta_{\mathrm{ref}} = 100$ are shown in Figure 4. The model evolutions begin with an initial transient stage, marked by an instabilities from the hot thermal boundary layer within 0.5 overturns and lasting 4-5 mantle overturns (approximately 200 model timesteps, but longer for some models), after which the model interiors enter a state of steady secular heating, secular cooling, or apparent thermal equilibrium. After the initial transient, the thermal boundary layer thicknesses become thinner for the hotter mantles, and distinct differences at the depth of the mantle transition zones ($z = 500$–700 km) are also apparent. The $1700\,\mathrm{K}$ and $1800\,\mathrm{K}$ models undergo 50–$100\,\mathrm{K}$ of secular heating in the mantles over more than twenty mantle overturns (maximum rate of 6.5 K/Gyr after the merging transient), and do not exhibit layering of cold, sub-lithospheric drips. The hotter models tend to initialize nearer to steady state, and they are more consistently layered along the mantle transition zone.

The extent to which a thermal disequilibrium *across* the mantle transition zone is maintained at any given time is quantified in Figure 5. In the bottom-heated models where $T_{\mathrm{pot,LM}} = 1750$–$1850\,\mathrm{K}$, the upper mantle potential temperatures are hotter than the lower mantle potential temperatures arising from an asymmetry in radial mantle flow.

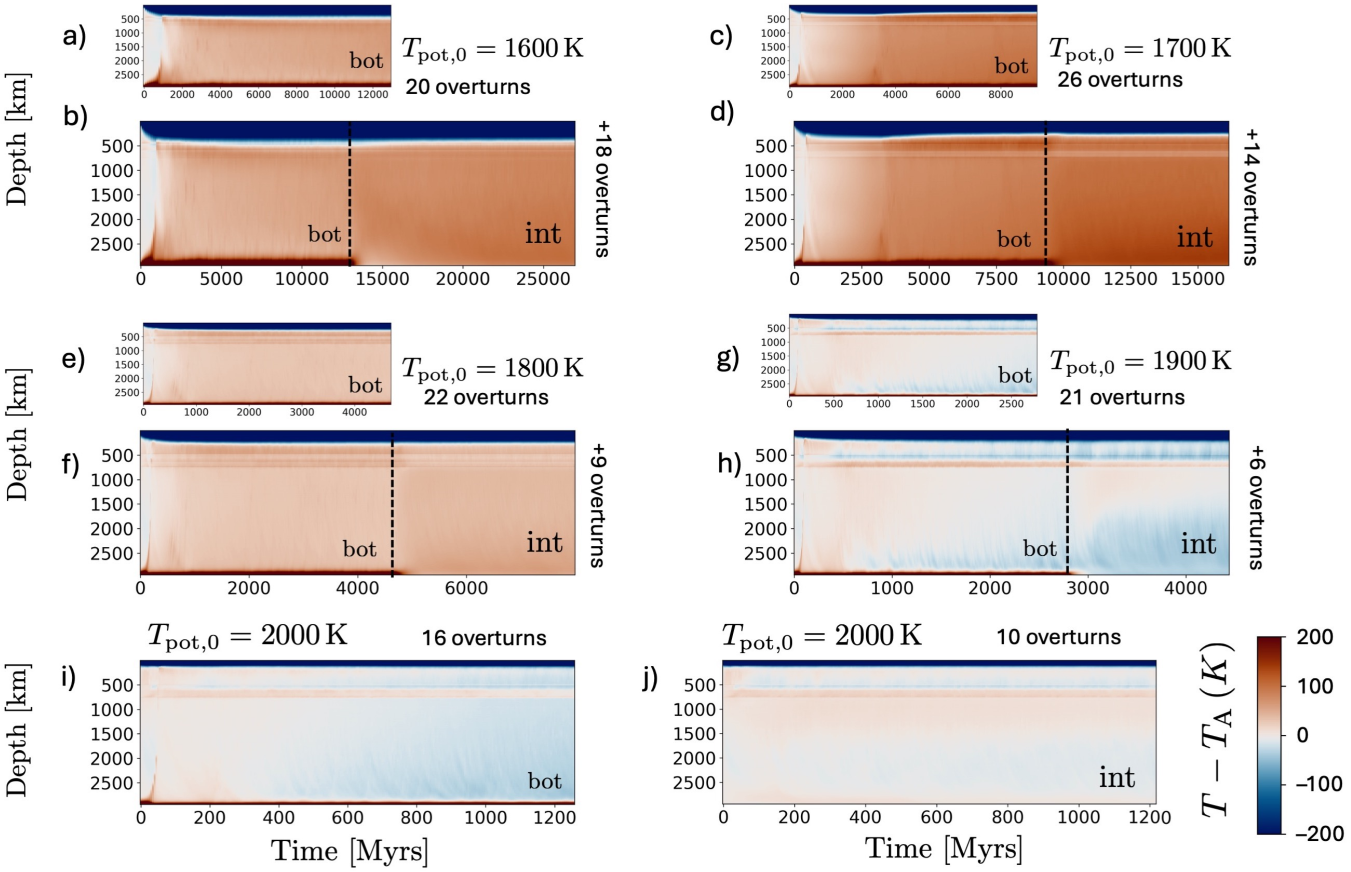

FIGURE 4 – These color-maps show the evolution of the azimuthally averaged temperature deviations from the initial mantle adiabat for a subset of models for which $\Delta\eta_{\mathrm{ref}} = 100$. The smaller figures (a,c,e,g) and (i) are purely bottom heated. The larger figures (b,d,f,h) are the same exact models as the corresponding smaller figure, but integrated further in time with purely internal heating and an insulated bottom boundary. The model in subplot (j) is initialized with internal heating and is not a continuation of the model in (i). The transition from bottom heated to internally heated is represented by the dotted black line and the volumetric heating rate is given in Table 2.

In this temperature range, cold drips do not tend to layer in the MTZ but hot plumes from the CMB can pass through the MTZ and the material stays in the upper mantle due to its positive thermal buoyancy and heats this region. This effect is largely diminished in the internally heated models in Figure 5b due to the lack of core heating and thus the lack of sustained mantle plumes with high thermal buoyancy originating from CMB depths. In all models where $T_{\mathrm{pot,LM}} = 1850$–$1950\,\mathrm{K}$, the cold drips layer more effectively at the MTZ, and their collective ponding keeps the upper mantle cool with respect to the lower mantle temperatures. Beyond $T_{\mathrm{pot,LM}} = 1950\,\mathrm{K}$, the difference in temperature between the upper and lower mantle specific entropies appear negligible and the upper and lower mantles appear to be better equilibrated than in the 1900 K models.

Histogram distributions and profiles of the conductive surface heat flux are shown in Figure 6 to characterize the heat flow variability at the final timestep of the bottom heated models. We note that the heat fluxes measured do not incorporate any volcanism-related component of surface heat flow and are purely conductive values. For mantle temperatures of $1900\,\mathrm{K}$ and higher, the shape of the heat flux distribution broadens, indicating the heat flux in warmer models have a higher variability than the colder models (i.e., < 1850 K). This broadening in the surface conductive heat flux for the hotter models coincides with the consistent mantle layering punctuated by avalanches (Figure 4) as well as the equilibration of the upper and lower mantle convective systems (Figure 5).

An "estimate" of the surface heat flow in TW at the final timestep can be made with an evenly spaced array of surface heat fluxes along the circumference of the domain, the outer surface. Multiplying mean surface heat fluxes and respective standard deviations (from evenly spaced sampling along the surface) by the surface area of a 3D sphere with $R_p = 6052$ km, the surface heat flows for the models are in Table 3. However, these 3D estimates for our 2D models are limited by the biases of reduced-dimensionality models (*Fleury et al.*, 2024). To correct for 2D cylindrical models having a 46% greater surface temperature gradient than equivalent 3D spherical models (*Fleury et al.*, 2024, Figure 3) each of the TW heat flows can be divided by 1.46. The outcome of this correction factor on the surface heat flow is shown in Table 3. The variabilities in the surface heat flux along the outward half-circumference of the domain are shown in Figure 6c-d as variability in the lithosphere thicknesses is pronounced due to its thinning in the hotter models. The evolution of the mean surface heat fluxes for the bottom-heated $\Delta\eta_{\mathrm{ref}} = 100$ model are in Figure 6e.

The magnitude and variation of core heat fluxes are shown in Figure 7 for the eight bottom-heated models for which $\Delta\eta_{\mathrm{ref}} = 100$. For most models the temperature contrast across the CMB was $\approx\ 600$ K; however, the resulting

Model	$T_{\text{pot,LM}}$ [K]	Surface heat flow (meas.) [TW]	Surface heat flow (corr.) $(Q/1.46)$ [TW]
1600K-30x	1704	6.7 ± 1.0	4.6 ± 0.7
1600K-100x	1642	5.2 ± 1.4	3.6 ± 1.0
1700K-30x	1810	10.7 ± 0.7	7.3 ± 0.5
1700K-100x	1765	8.7 ± 1.3	6.0 ± 0.9
1800K-30x	1848	11.9 ± 1.6	8.2 ± 1.1
1800K-100x	1818	10.1 ± 1.5	6.9 ± 1.0
1900K-30x	1919	15.7 ± 2.2	10.8 ± 1.5
1900K-100x	1891	13.0 ± 2.2	8.9 ± 1.5
2000K-30x	2000	24.9 ± 2.3	17.1 ± 1.6
2000K-100x	1982	22.7 ± 2.6	15.5 ± 1.8
1860K-100x	1845	8.9 ± 1.4	6.1 ± 1.0
1950K-100x	1958	19.8 ± 2.8	13.6 ± 1.9
2050K-100x	2023	25.2 ± 2.2	17.3 ± 1.5
1600K-100x-int	1663	5.6 ± 0.5	3.8 ± 0.3
1700K-100x-int	1779	8.7 ± 0.6	6.0 ± 0.4
1800K-100x-int	1827	10.3 ± 0.5	7.1 ± 0.3
1900K-100x-int	1884	12.8 ± 0.7	8.8 ± 0.5
2000K-100x-int	1994	23.9 ± 2.1	16.4 ± 1.4

TABLE 3 – Lower mantle potential temperatures, 3D estimated heat flows, and corrected 3D estimated heat flow for the final timestep of each model using a correction factor determined by the results of *Fleury et al.* (2024)

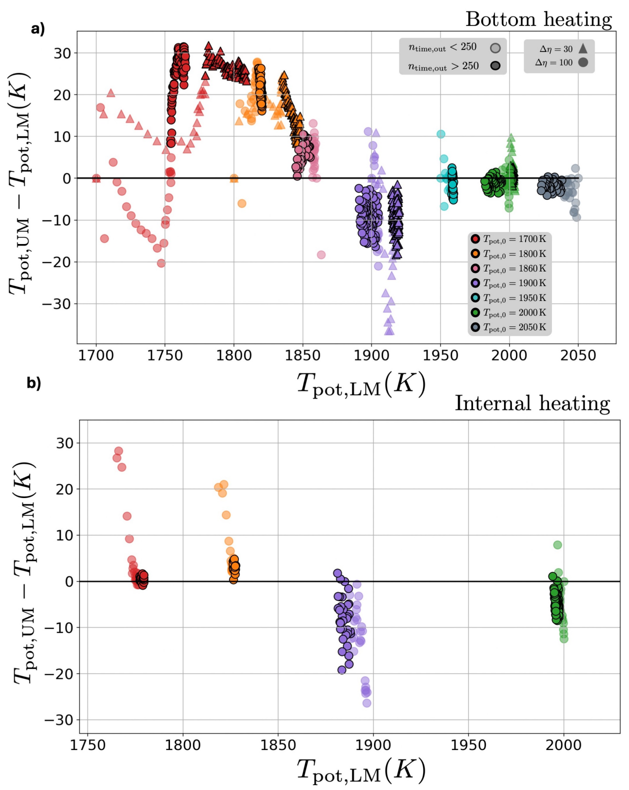

FIGURE 5 – These scatter plots (a) for bottom heated models and (b) for internally heated models) show the difference in the mantle potential temperatures between the upper and lower mantle regions. Each point represents a sampled timestep (n) in the model evolution. The term $n_{\text{time,out}}$ represents the integer number of timesteps output as a mesh (i.e., recorded as points on this plot) at that stage of the model evolution.

core heat fluxes vary due to changes in the lower mantle temperature over time. A "gap" can be seen between the $1900\,\text{K}$ and $1800\,\text{K}$ evolution plot in Figure 7c indicating that the ΔT driving heat flow from the core increases for the higher-temperature mantles due to the general cooling trend of the mantle temperature as well as the cold mantle avalanches from the MTZ which carry large masses of cold material to the CMB, sharply increasing the temperature gradient and thus heat flux regionally. The plot in Figure 7a shows that core heating is more variable in the hotter models than the cooler models, especially the $1700\,\text{K}$ model with a narrower distribution of core heat fluxes compared to other models. Figure 7c also shows the prolonged initial transient state of the $1700\,\text{K}$ model (red line); the initial plumes do not merge into their lower degree stable configuration until after ten mantle overturns.

A log-log plot of the Rayleigh number versus the Nusselt number is shown in Figure 8 as in Equation (13) for all models where $\Delta\eta_{\text{ref}} = 100$. We display the values of a' and β' in Figure 8b for each of the 13 total models such that the fit of the power law along the model's steady evolution has a coefficient of determination $r^2 > 0.4$. The prime notation indicates the power law scaling parameters for a single model. These individual scaling laws capture the trends in models undergoing long-term secular heating and cooling, with rates decreasing at further points in the evolutions (see Supplemental Figures). We have added the $1860\,\text{K}$, $1950\,\text{K}$, and $2050\,\text{K}$ models for $\Delta\eta_{\text{ref}} = 100$ in addition to the models in *Kerr et al.* (2025) in order to better resolve the transition in the Rayleigh-Nusselt scaling. Plots in Figure 8c-e show a snapshot at the final timestep for the $1800\,\text{K}$, $1900\,\text{K}$, and $2000\,\text{K}$ models with $\Delta\eta_{\text{ref}} = 100$. Comparing the eight $\Delta\eta_{\text{ref}} = 100$ models in concert, the models with initial temperatures of $1600\,\text{K}$, $1700\,\text{K}$, $1800\,\text{K}$, and $1900\,\text{K}$ seemed to collectively follow a $\beta = 1/3$ scaling exponent; however, the $1700\,\text{K}$ model appears to increase in heat flux rapidly with small changes to its Rayleigh number. The $1950\,\text{K}$, $2000\,\text{K}$, and $2050\,\text{K}$ models deviate from the black dotted line and seemingly follow a high Nu trend of the same slope, indicating a shift to higher-than-expected Nusselt number for that given Rayleigh number.

The plots in Figure 9 combines Equations (8) and (14), using the lower mantle region between 50 and 90 GPa to compute the Rayleigh number from the thermophysical properties and the temperature-dependent viscosity correction using θ. Using this formulation, the single-model

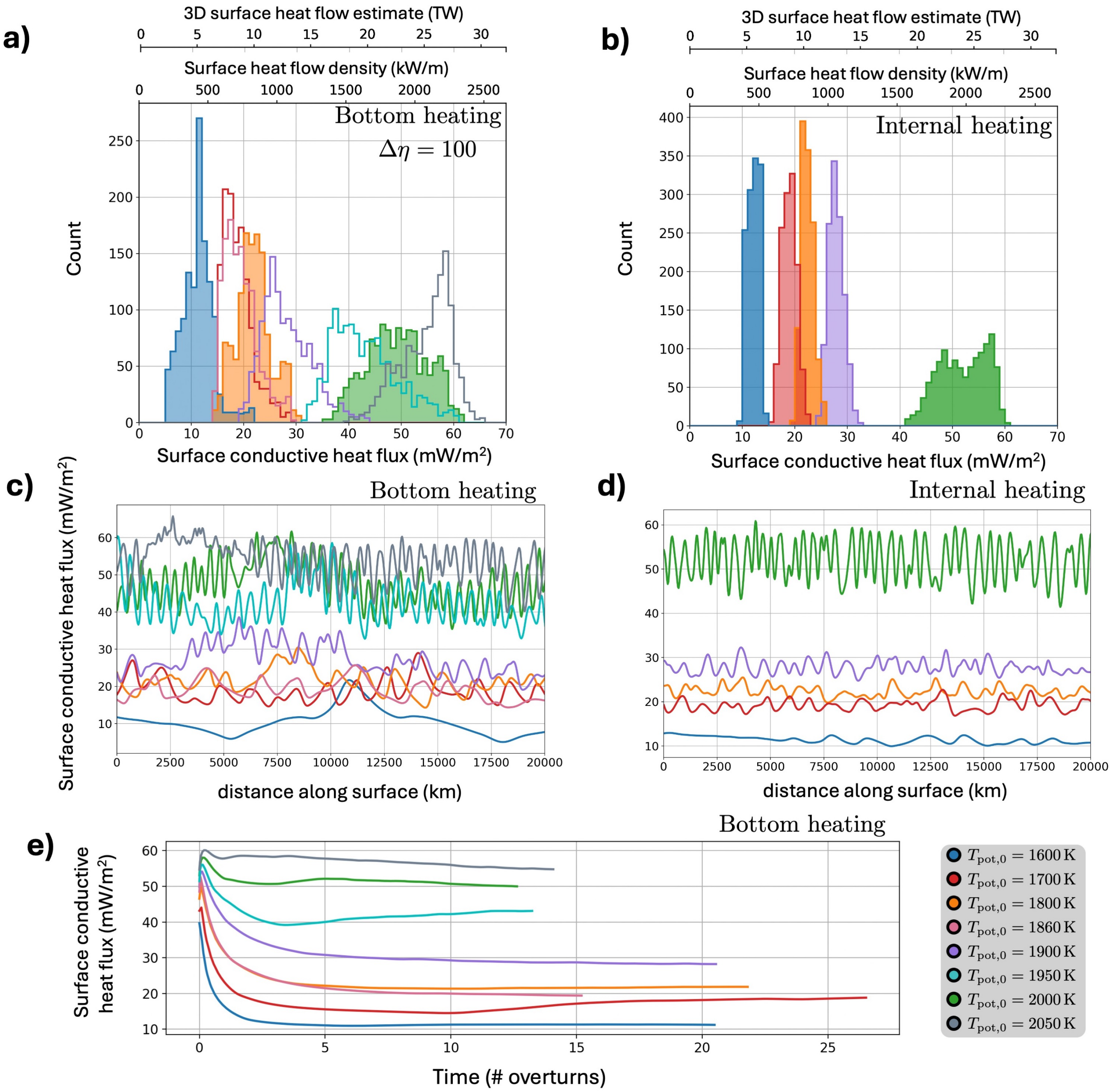

FIGURE 6 – Histograms of the surface heat flux distribution at the final timestep of the bottom-heated (a) and internally-heated (b) $\Delta\eta_{\mathrm{ref}} = 100$ models. In (c) and (d) are half-circumference segments for along-surface profiles of the heat flux for bottom- and internally-heated models, respectively. The time evolution of the mean surface conductive heat flux for bottom-heated $\Delta\eta_{\mathrm{ref}} = 100$ models are in (e).

Rayleigh-Nusselt scaling exponents β' in Figure 9b vary mostly above a value of $1/3$ and again are especially high for the $1700\,\mathrm{K}$ bottom-heated models. The same "jump" in the Nusselt number above $1900\,\mathrm{K}$ appears in the purely internally-heated model suite as well. Accounting for the strong temperature dependence of viscosity and two end-member modes of heating, the elevated Nusselt numbers for higher mantle temperatures and Rayleigh numbers persist.

The plots in Figure 10 combines Equations (9) and (14), using the upper mantle region between 10 and 15 GPa to compute the Rayleigh number. Using this formulation, the single-model Rayleigh-Nusselt scaling exponents β' in Figure 10b are all much closer to a value of $1/3$ regardless of which side of the "jump" that particular model is on. The pattern of anomalously high Nusselt numbers for Rayleigh numbers in mantles hotter than $1900\,\mathrm{K}$ remains in this formulation as well, despite the individual scaling exponents becoming closer to the boundary layer theory value of $1/3$ for Boussinesq, infinite Prandtl number models. Both the internally- and bottom-heated models in Fig. 10(a,c) show a similar shape in the Ra-Nu-θ plots: the $1800\,\mathrm{K}$ model juts out to higher Rayleigh numbers due to sharp variations locally in the thermo-physical properties (in this case, the mean thermal expansivity along the $1800\,\mathrm{K}$ adiabat). Otherwise, the Ra_2 formulation of Equation (14) shows an upwards shift for temperatures hotter than $1900\,\mathrm{K}$.

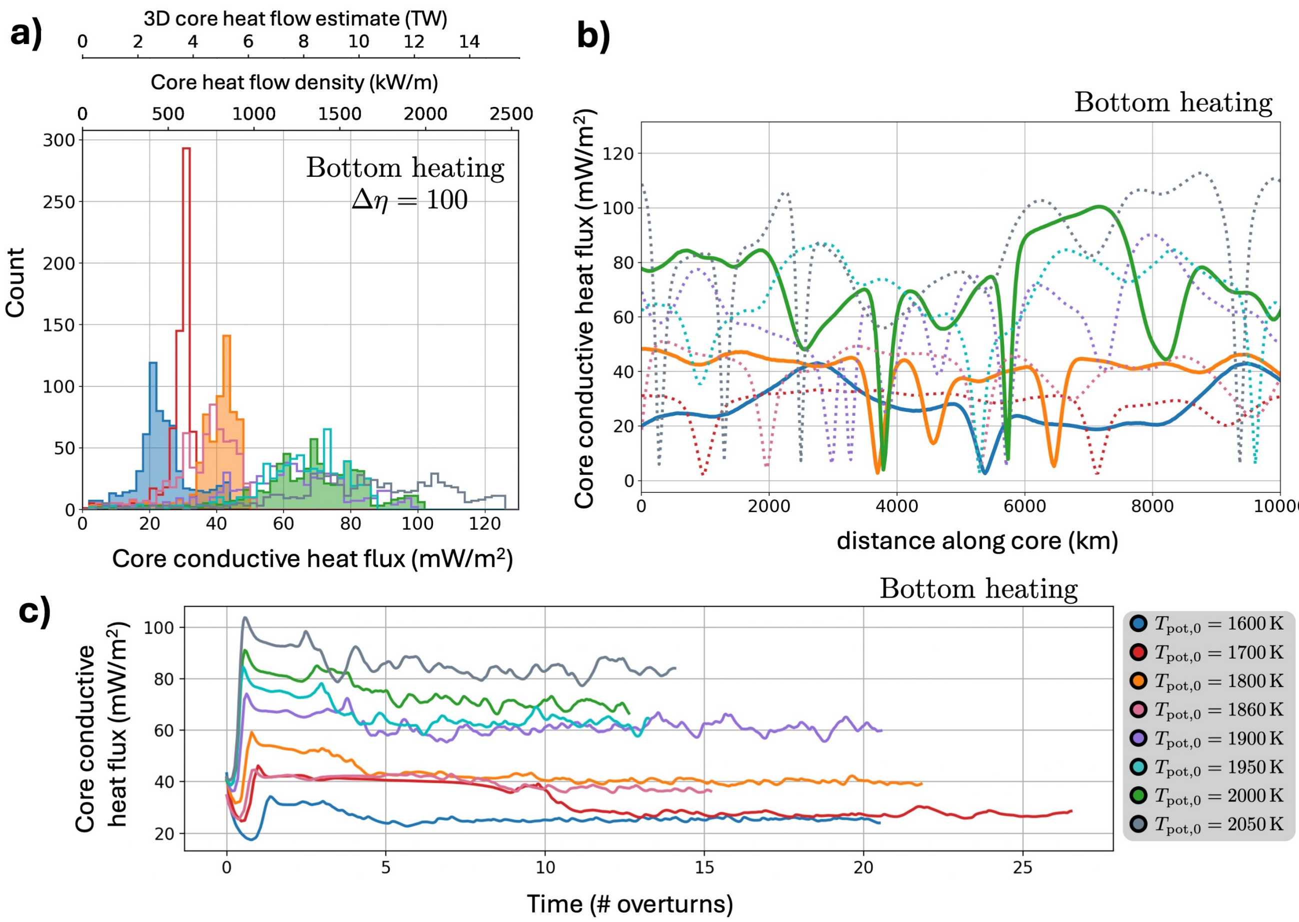

FIGURE 7 – A histogram of the core-mantle boundary heat flux distribution at the final timestep of the bottom-heated $\Delta\eta_{\mathrm{ref}} = 100$ models (a). In (b) are half-circumference segments for along-surface profiles of the core heat flux. The time evolution of the mean core conductive heat flux for bottom-heated $\Delta\eta_{\mathrm{ref}} = 100$ models are in (c).

We additionally explore scaling laws relating Rayleigh number and characteristic velocity for these systems in order to better understand the cause of the upward shift in Nusselt numbers and perhaps its relation to mantle layering and mineral phase transitions. These velocities are different from surface velocities within the lithosphere which we discuss in the Supplemental Information: Appendix A. We examine the root-mean-squared velocities in the upper mantle and lower mantle and compare them to the Rayleigh numbers computed for these regions (see Figure 11). The characteristic velocity of a convecting region scales with the Rayleigh number as $Ra^{2/3}$ from boundary layer theory for isoviscous fluid with infinite Prandtl number (*Siggia*, 1994). Since we are interested in the well-mixed regions of $10-15$ GPa and $50-90$ GPa, the isoviscous approximation of boundary layer theory should hold if the natural velocity of plumes rising and sinking due to thermal buoyancy is what drives mass flow through those regions. In the lower mantle (see Figure 11a, 11b), the RMS velocity scales with the viscosity-adjusted Rayleigh number with exponent of 0.643 and 0.671 for bottom and internally-heated systems, respectively. In the upper mantle, the scaling between velocity and Rayleigh number is much more irregular. In Figure 11c the velocity relates to Rayleigh number over θ with an exponent of 0.87 (not annotated), but splitting the suite of models into those starting at $1900\,\mathrm{K}$ and colder and those starting hotter than $1900\,\mathrm{K}$, we get two scaling exponents for these respective regions: 0.526 for the colder models and 1.42 for the hotter models.

In Figure 11(a,b) the scaling seems consistent throughout the models in concert. In Figure 11(c,d) the velocities are higher for models hotter than $1900\,\mathrm{K}$ (i.e., in a layered regime with frequent avalanches) than the upper mantle Rayleigh numbers based on thermo-physical properties should imply. The dynamics of mantle avalanches and their return flow induce upper mantle velocities faster than the cold thermal boundary layer can generate via natural thermal convection. In summary, the metric describing convective vigor due to thermal buoyancy (Ra) is not a good predictor for the characteristic velocity v_{rms} in the upper mantle region . This appears to be the case for both bottom-heated and internally-heated models.

Lastly, in Figure 12 we show the vertical mass flux $j = \rho v_z$ along the depth of $600\,\mathrm{km}$ which is near the center of the MTZ. As the temperature increases between $\approx 1620\,\mathrm{K}$ and $1700\,\mathrm{K}$, the mass flux through the MTZ increases as well. Between $1700\,\mathrm{K}$ and $\approx 1880\,\mathrm{K}$, the mass flux appears to even out because of the inhibiting effect of the WMF endothermic phase transition. Between $\approx 1880\,\mathrm{K}$ and $\approx 1930\,\mathrm{K}$, the mean mass flux appears to remain even with that of models between $1750\,\mathrm{K}$ and $1850\,\mathrm{K}$. However, the variability of the mass flux becomes much higher. Beyond $\approx 1930\,\mathrm{K}$ the mass flux through the transition zone increases again. Fig-

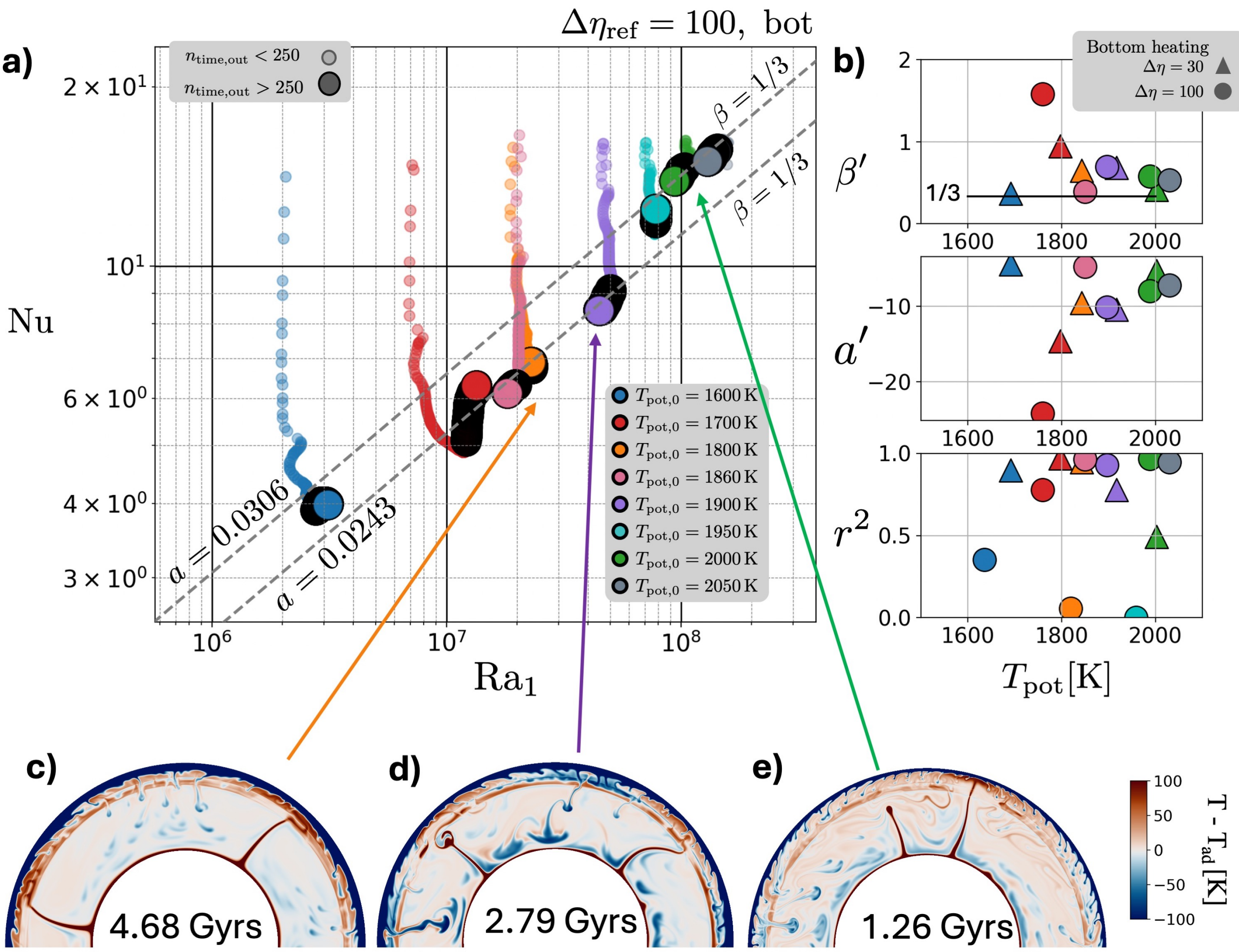

FIGURE 8 – Ra_1-Nu scaling (Equations (8) and (13)) in (a). Individual model scaling parameters are shown in (b) if $r^2 > 0.4$. Plots (c)-(e) highlight the non-adiabatic temperature field at the final timestep of the 1800 K, 1900 K, and 2000 K models with $\Delta\eta_{\mathrm{ref}} = 100$. In (a), each circle represents the Ra_1-Nu for a single timestep: large circles indicate snapshots after the plume-merging transient period ($n_t < 250$) and small circles indicate that transient period. The dotted gray lines have a slope of 1/3 in log-log space for reference and are pinned to the final timesteps of the 1800 K and 2000 K models.

ure 4i-j and Figure 8e demonstrate that at $2000\,\mathrm{K}$ the model is still in a regime of layering and exhibits avalanches, yet as the models become hotter between $1900\,\mathrm{K}$ and $2000\,\mathrm{K}$, the mass flux between the lower and upper mantles increases, equilibrating the potential temperatures (Figure 5). Our observation that increasingly hotter mantles with endothermic phase transitions create less strong layering in the transition zone is counterintuitive. In the following section, we will explain how a more realistic description of the equation of state for pyrolite can cause this counterintuitive behavior and discuss the impact this finding may have on planetary cooling and our understanding of the present-day state of the planet Venus.

5 Discussion

Previously published research regarding the dynamics of mantle convection with endothermic mineral phase transitions generally supports the notion that for a fixed negative Clapeyron slope $\gamma = dP/dT$ of a phase transition, as the Rayleigh number increases, the convective length scale decreases and the ability for the endothermic phase transition to *inhibit* mass flow from the thermal upwellings or downwellings is promoted (*Christensen and Yuen*, 1984; *Wolstencroft and Davies*, 2011). Rayleigh number changes are dominantly driven by changes in mantle temperature which strongly reduce the viscosity due to the exponential dependence of viscosity on temperature. In prior studies (e.g., *Christensen and Yuen*, 1985; *Solheim and Peltier*, 1993; *Yuen et al.*, 1994, 1995; *Tackley*, 1996; *Bunge, H.-P. et al.*, 1997), a useful rule-of-thumb emerges: for a given endothermic phase transition of a fixed Clapeyron slope and thickness, if the Rayleigh number increases, the time-averaged mass flux across the transition zone decreases. However, this prior research did not elaborate in great depth on the conditions of a stagnant-lid planet despite temperature-dependent viscosity conditions applied within the subducting slabs (e.g., *Christensen and Yuen*, 1984).

Figure 12 shows how our simulations appear to contradict this prior wisdom. In Figure 5, the temperature equilibration between the upper and lower mantle for $T_{\mathrm{pot}} > 1900\,\mathrm{K}$ implies there is sufficient mass exchange between the upper and lower mantles. Figure 3a, however, shows the $1900\,\mathrm{K}$ models and $2000\,\mathrm{K}$ models both passing through the WMF zone. That the higher mantle temper-

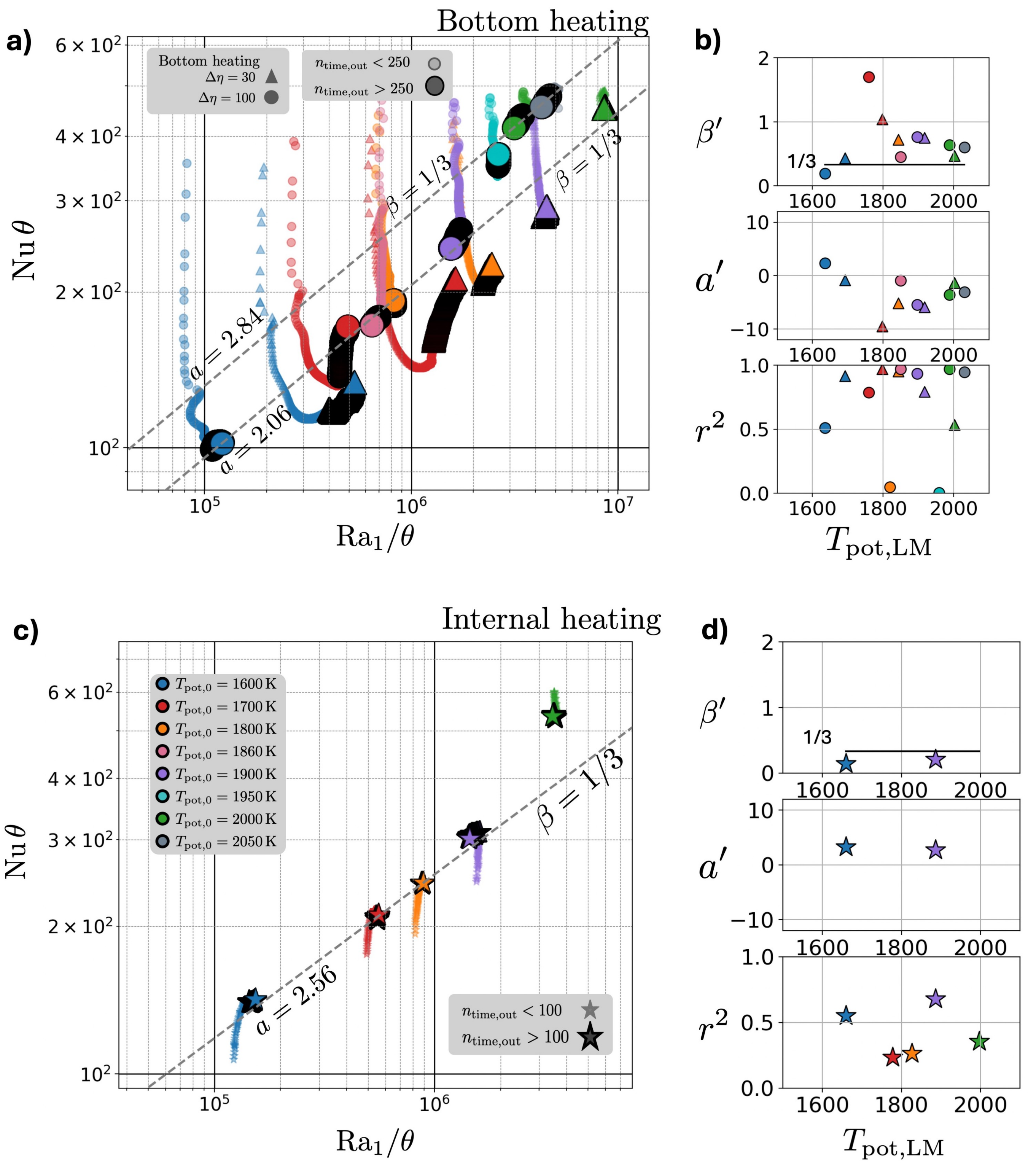

FIGURE 9 – Ra_1-Nu scaling (Equations (8) and (14)) in (a) for bottom heated models with $\Delta\eta_{\mathrm{ref}} = 100$ (circles) and $\Delta\eta_{\mathrm{ref}} = 30$ (triangles). Individual scaling parameters in (b). The same Ra-Nu-θ formulations in (c) and (d) for the purely internally-heated models. The dotted gray lines have a slope of 1/3 in log-log space for reference and are pinned to the final timestep of the 1800 K and 2000 K models respectively.

atures and thus Rayleigh numbers of the $\approx 2000\,\mathrm{K}$ models induce *more* mass flow through the MTZ than the colder $1900\,\mathrm{K}$ models warrant further investigation. We will do our best to explain the reasoning for this result and discuss the implications of this result in the context of our Rayleigh-Nusselt scaling plots and Rayleigh-velocity scaling plots.

5.1 How hotter temperatures weaken mantle layering

Examining the geometry of the WMF zone in Figure 2a shows this transition is more complex than a simple line with a negative Clapeyron slope γ dividing two materials of different densities. The long kite-like quadrilateral shape of the WMF zone is generally aligned with a negative slope; however, the WMF region is broad, and the adiabats of mantles we simulate intersect and crosscut this region such that the

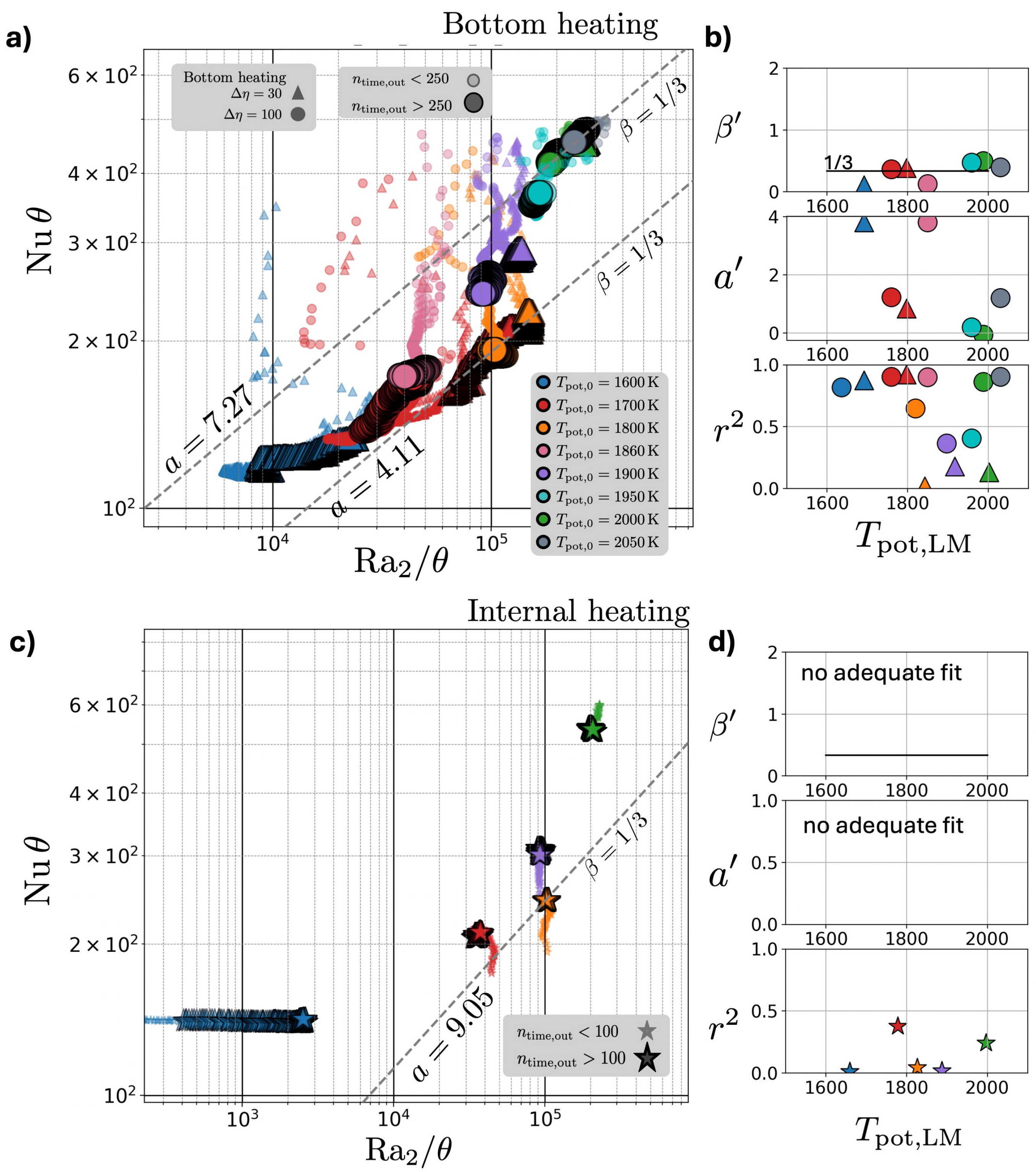

FIGURE 10 – Ra_2-Nu scaling (Equations (9) and (14)) in (a) for bottom heated models with $\Delta\eta_{\mathrm{ref}} = 100$ (circles) and $\Delta\eta_{\mathrm{ref}} = 30$ (triangles). Individual scaling parameters in (b). The same Ra-Nu-θ formulations in (c) and (d) for the purely internally-heated models. The dotted gray line has a slope of 1/3 in log-log space for reference.

phase transition zone boundaries, not the phase transitions themselves, have positive or negative slopes through P–T space. Take the $1900\ \mathrm{K}$ model, for example, and examine the cartoon schematic in Figure 11a, which replicates and simplifies the color map of pyrolite thermal expansivity in Figure 2a. The $1900\ \mathrm{K}$ adiabat passes near the 'corner' of the quadrilateral where colder material typical for cold drips ($\sim\ 100\ \mathrm{K}$ colder than the adiabat) encounters a positive slope. As cold drips slow and stagnate at a given pressure (dark blue icons in Figure 11a), they also become more diffuse and warmer, shifting them 'rightward' (hotter) in P–T space. While the drips get warmer, wadsleyite is converted into the denser majorite and ferropericlase phases; the effective negative thermal expansivity inside the WMF zone results in a net neutral/positive buoyancy for the material.

Figure 11b shows a schematic for the $2000\ \mathrm{K}$ adiabat

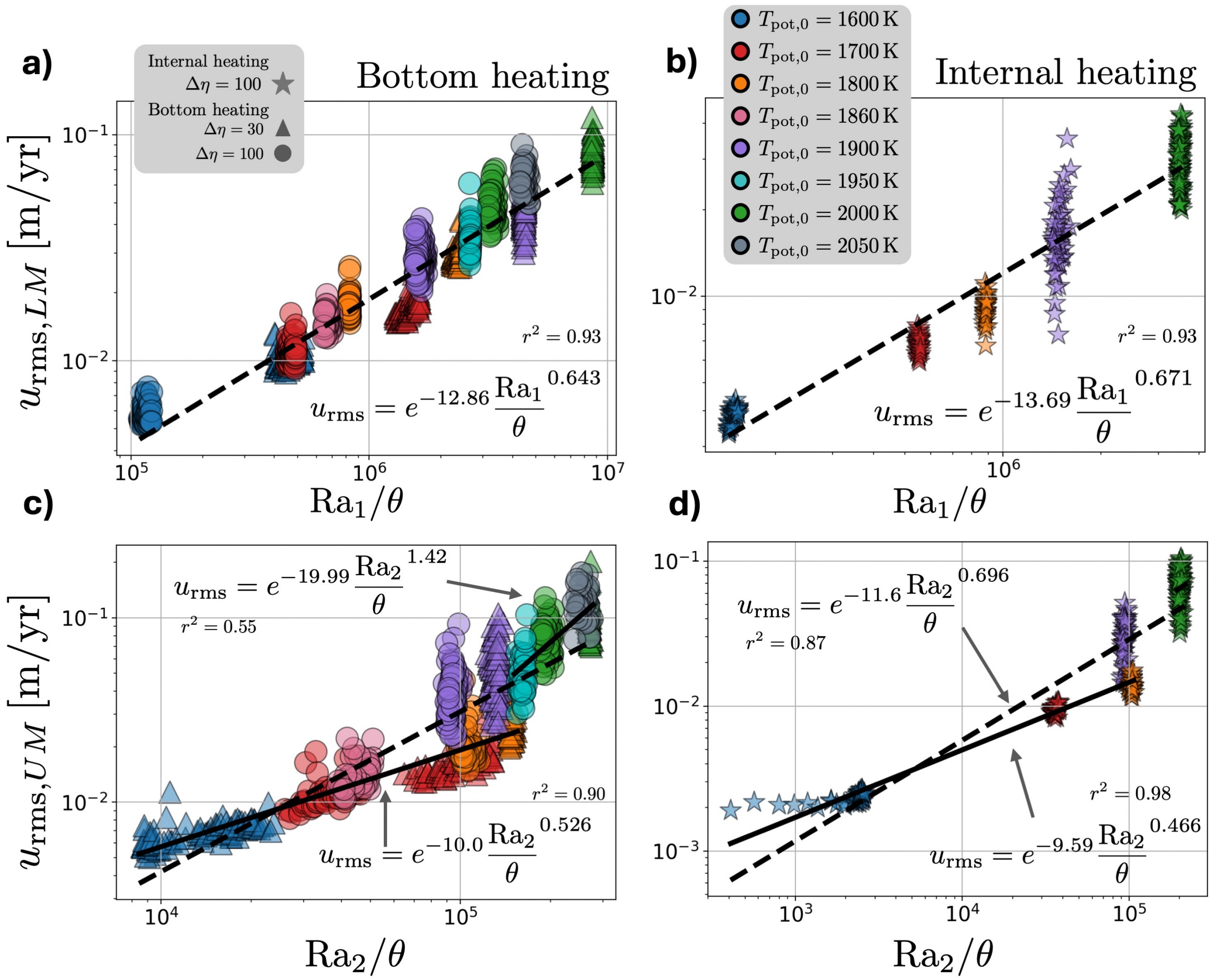

FIGURE 11 – The relationship between the lower mantle (a,b) and upper mantle (c,d) Rayleigh number and the root-mean-squared velocity in that region for the bottom-heated (a,c) and internally-heated (b,d) models separately.

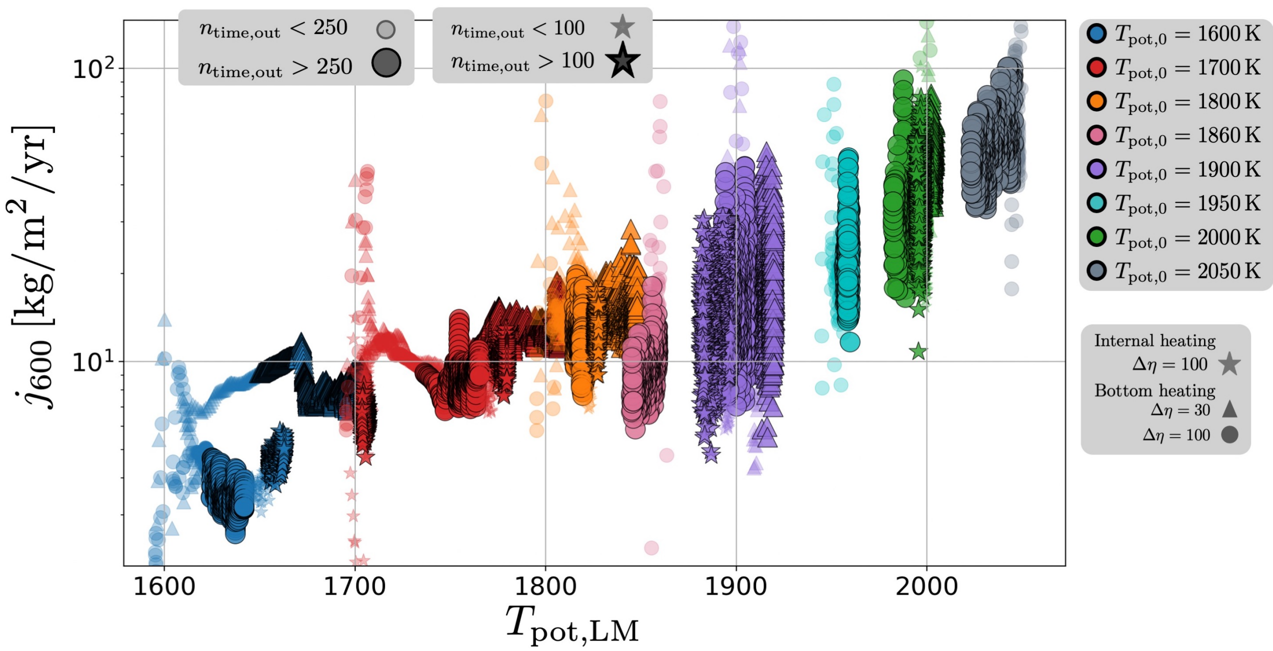

FIGURE 12 – This figure show a scatter plot of the mass flux across the depth of 600 km in kg/m2/yr/. Each data point is represents the mean mass flux at 600 km depth for a given timestep. Every 10th timestep is shown for ease of visualization.

Model	$u_{\rm rms}^{\rm UM}$ [m/yr]*	$u_{\rm rms}^{\rm LM}$ [m/yr]*	$\lvert u\rvert$ [m/yr]*	Pe *	$\#$o.t.	$\tau_{\rm o.t.}$ [Myrs]	t_f [Myrs]	$d_{\rm SL}$ [m]*	Di
1600K-30x	7.76e-3	1.10e-2	7.87e-3	0.533	32.0	374	1.19e4	2.997e5	0.370
1600K-100x	3.75e-3	5.90e-3	4.66e-3	3.43	20.5	632	1.29e4	3.86e5	0.369
1700K-30x	1.82e-2	1.86e-2	1.41e-2	0.158	36.2	209	7.55e3	1.96e5	0.371
1700K-100x	1.24e-2	1.13e-2	8.33e-3	0.475	26.5	353	9.35e3	2.42e5	0.371
1800K-30x	2.80e-2	3.11e-2	2.42e-2	0.379	34.1	121	4.13e3	1.85e5	0.372
1800K-100x	2.09e-2	1.77e-2	1.37e-2	0.908	21.8	215	4.68e3	2.13e5	0.372
1900K-30x	5.68e-2	5.10e-2	3.65e-2	0.437	24.8	80.5	2.00e3	1.47e5	0.374
1900K-100x	4.00e-2	2.95e-2	2.17e-2	0.852	20.6	136	2.79e3	1.75e5	0.374
2000K-30x	1.15e-1	8.41e-2	6.51e-2	0.749	17.9	45.2	805	9.70e4	0.375
2000K-100x	8.35e-2	4.74e-2	3.84e-2	0.787	16.4	76.7	1.26e3	1.06e5	0.375
1860K-100x	1.37e-2	1.48e-2	1.17e-2	0.723	15.2	252	3.83e3	2.51e5	0.373
1950K-100x	5.08e-2	3.60e-2	2.58e-2	0.454	13.2	114	1.51e3	1.20e5	0.375
2050K-100x	1.20e-1	6.41e-2	5.28e-2	1.01	14.1	55.8	785	9.71e4	0.376

TABLE 4 – Some dynamics diagnostics for bottom-heated models. Starred quantities indicate an average value over roughly the final two overturns (o.t.) of the model evolution (100 time-steps). $u_{\rm rms}^{\rm UM}$ is the upper mantle root mean squared velcoity, $u_{\rm rms}^{\rm LM}$ is the lower mantle root-mean-squared velocity, $\lvert u\rvert$ is the average magnitude of velocity vectors throughout the domain, Pe is the surface Péclet number, $\#\mathrm{o.t.}$ is the number of overturns where $\tau_{\rm o.t.}$ is the length of a single overturn. t_f is the final model time computed and $d_{\rm SL}$ is the stagnant lid thickness. Di is the dissipation number, defined by $gD\alpha/C_p$.

Model	$q_{\rm surf}\pm\delta_{q_{\rm surf}}$ [W/m^2]	$q_{\rm cmb}\pm\delta_{q_{\rm cmb}}$ [W/m^2]	$Q_{\rm surf}$ [W/m]	$Q_{\rm cmb}$[W/m]	$T_{\rm pot}^{\rm LM}$ [K]	$T_{\rm pot}^{\rm UM}$ [K]
1600K-30x	0.0144 ± 0.00215	0.0296 ± 0.00762	5.48e5	5.79e5	1703	1695
1600K-100x	0.0113 ± 0.00308	0.0253 ± 0.00836	4.29e5	4.95e5	1640	1518
1700K-30x	0.0232 ± 0.00162	0.0355 ± 0.00802	8.82e5	6.93e5	1808	1833
1700K-100x	0.0187 ± 0.00260	0.0272 ± 0.00506	7.10e5	5.31e5	1764	1793
1800K-30x	0.0257 ± 0.00357	0.0577 ± 0.0136	9.78e5	1.13e6	1848	1860
1800K-100x	0.0219 ± 0.00331	0.0396 ± 0.00828	8.31e5	7.74e5	1819	1839
1900K-30x	0.0340 ± 0.00487	0.0792 ± 0.0254	1.29e6	1.55e6	1920	1910
1900K-100x	0.0283 ± 0.00458	0.0620 ± 0.0189	1.08e6	1.21e6	1892	1884
2000K-30x	0.0542 ± 0.00489	0.0939 ± 0.0236	2.06e6	1.84e6	2001	2003
2000K-100x	0.0495 ± 0.00567	0.0687 ± 0.0167	1.88e6	1.34e6	1983	1981
1860K-100x	0.0195 ± 0.00280	0.0367 ± 0.00913	7.42e5	7.17e5	1846	1850
1950K-100x	0.0431 ± 0.00610	0.0626 ± 0.01599	1.64e6	1.22e6	1959	1959
2050K-100x	0.0550 ± 0.00465	0.0844 ± 0.0239	2.09e6	1.65e6	2025	2023

TABLE 5 – Thermal diagnostics for bottom-heated models. All quantities are an average value over roughly the final two overturns (o.t.) of the model evolution (100 time-steps). Heat fluxes are denoted by q and heat flow densities by Q. The δ indicates uncertainty by giving the average value of the standard deviation of q around the domain at each of the final 100 timesteps.

Model	$u_{\rm rms}^{\rm UM}$ [m/yr]*	$u_{\rm rms}^{\rm LM}$ [m/yr]*	$\lvert u\rvert$ [m/yr]*	Pe *	$\#$o.t.	$\tau_{\rm o.t.}$ [Myrs]	t_f [Myrs]	$d_{\rm SL}$ [m]*	Di
2000K-int	6.94e-2	3.07e-2	2.31e-2	0.124	9.56	127	1.22e3	1.01e5	0.375
1900K-int	2.75e-2	1.51e-2	1.01e-2	0.175	5.66	292	4.44e3	1.76e5	0.374
1800K-int	1.49e-2	9.34e-3	8.28e-3	0.230	9.30	355	7.99e3	2.08e5	0.372
1700K-int	9.65e-3	6.80e-3	5.97e-3	0.775	13.83	493	1.61e4	2.41e5	0.371
1600K-int	2.56e-3	4.03e-3	3.70e-3	3.36	17.60	795	2.69e4	3.58e5	0.369

TABLE 6 – Dynamic diagnostics for internal heating models. Starred quantities indicate an average value over roughly the final two overturns (o.t.) of the model evolution (100 time-steps).

Model	$q_{\rm surf}\pm\delta_{q_{\rm surf}}$ [W/m^2]	$Q_{\rm surf}$ [W/m]	$T_{\rm pot}^{\rm LM}$ [K]	$T_{\rm pot}^{\rm UM}$ [K]
2000K-int	0.0521 ± 0.00443	1.98e6	1995	1991
1900K-int	0.0280 ± 0.00157	1.06e6	1882	1874
1800K-int	0.0224 ± 0.00122	8.53e5	1827	1830
1700K-int	0.0188 ± 0.00135	7.16e5	1779	1780
1600K-int	0.0121 ± 0.00107	4.60e5	1662	1569

TABLE 7 – Thermal diagnostics for internal heating models. All quantities are an average value over roughly the final two overturns (o.t.) of the model evolution (100 time-steps).

and the behavior of ponding sub-lithospheric drips as they warm toward the ambient mantle temperature. At a given depth, the drips $\sim\ 100\ \mathrm{K}$ cooler than the mantle adiabat accumulate and begin to absorb heat from the surrounding fluid. Since these drips are in the WMF phase region, heating them makes them denser. However, the boundary between the effective negative and effective positive thermal expansivity regions exists along that isobar in the direction of temperature increase. The cold layered drips warm up enough to convert all the wadsleyite (less-dense phase) into majorite and ferropericlase (denser phases). The even warmer ambient mantle at that pressure is completely composed of the denser phases, so the system reverts to a "normal" sense of thermal buoyancy where the cold drips can now sink through the ambient mantle. The ability of the WMF zone to accommodate additional cold drips near the $2000\ \mathrm{K}$ adiabat is reduced compared to the $1900\ \mathrm{K}$ adia-

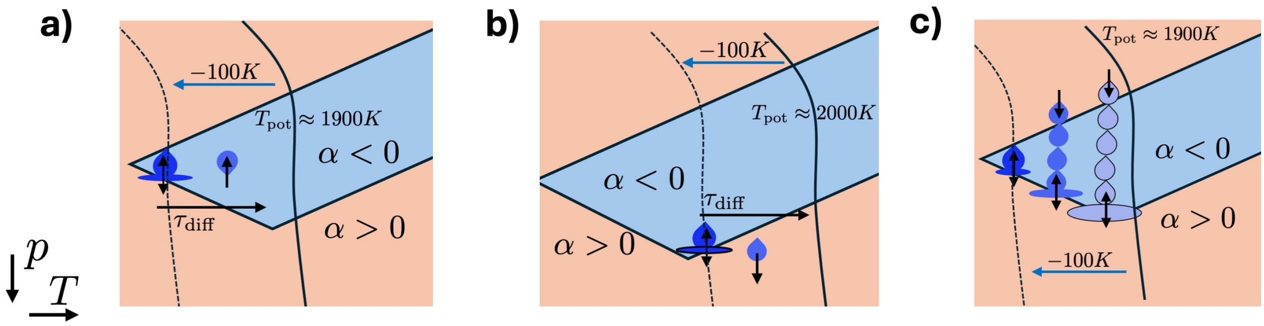

FIGURE 13 – A cartoon schematic of the thermal expansivity coefficient phase diagram such as the one shown in Figure 1 and Figure 3. This schematic might explain how in a complex mantle transition zone hotter mantles with higher Rayleigh numbers and smaller plume heads can layer less effectively than colder mantles. The curved line in (a) represents a $1900\,\mathrm{K}$ adiabat and the dotted line represents material about $-100\,\mathrm{K}$ from the adiabat. In (b) the mantle is shifted to warmer temperatures and the geometry of the phase transition boundary changes. Panel (c) is a continuation of (a) showing that instead of rising, the cold drips in the $1900\,\mathrm{K}$ models are in a balance of forces: the positive phase buoyancy pointing up and the normal force from the pile of cold drips above the phase transition pointing down.

bat since cold drips heating toward the mean mantle temperature revert more readily to a "normal" sense of thermal buoyancy.

However, an explanation for the system's dynamics needs to account for a continuous stream of drips falling from the base of the lithosphere, as shown in Figure 11c. The slowly warming layer of cold drips is pushed from above by newly arriving drips originating from the base of the lithosphere. Since this base-layer is warming diffusively, the lower boundary of the WMF zone is deflected to even higher pressures (i.e., deeper), allowing this base-layer to remain layered in the transition zone and accommodate more cold drips piling atop it. At the point of avalanche initiation, the downwards piling forces beat out the upwards phase buoyancy and push the bottom layer of drips into the positive thermal expansivity zone where they descend and entrain some of the cold drips into the lower mantle in a large flush event. The threshold for a flushing event is therefore higher in the $1900\,\mathrm{K}$ models since more drips can accumulate and pack into the MTZ as they slowly absorb heat from the surrounding mantle. Appendix H in the Supplementary Information discusses possible differences in the buoyancy experienced by cold drips across the WMF zone.

5.2 'Equilibrium' avalanches enhancing mantle heat flow

The primary result of this work is that we observe an increase in the surface heat flow with increasing Rayleigh number for mantle potential temperatures $T > 1900$ K compared to that for colder models ($1500\,K < T < 1900$ K) with the same mantle composition. This may seem counter-intuitive in two regards. First, the presence of an endothermic phase transition for the models with adiabats between $1700\,\mathrm{K}$ and $2050\,\mathrm{K}$ should generally hinder mass flow, and thus convective heat flow, from the lower mantle into the upper mantle. Second, the larger the Rayleigh number, the smaller the size of the plumes and the easier it should be for the phase transition to deflect the flow of these small plumes and layer them along the base of the WMF zone.

Mantle avalanches are typically thought of as infrequent, non-equilibrium events in a planet's thermal evolution, occurring over ~ 100 Myr "cycles" (*Herein et al.*, 2013). When the Clapeyron slope of the endothermic phase transition is large, the material can build up in stratified upper and lower mantle layers for longer. When the cold material of the upper mantle flushes through the transition zone, it does so more suddenly than if the material had not built up as long, or at all (i.e., when $\gamma > 0$) (*Yuen et al.*, 1995). It has been reported in previous numerical simulations of mantle avalanches that the resulting surface heat flux spikes due to the return flow of warm material into the upper mantle is greater in magnitude than the surface heat flux in cases where there are no endothermic phase transitions or avalanches (*Trubitsyn et al.*, 2008; *Yuen et al.*, 1995). However, due to the relative infrequency of these more "violent" events and their shorter duration, the time-averaged heat flux out of the surface either did not noticeably change (e.g., *Yuen et al.*, 1994), or a time-averaged Rayleigh-Nusselt relation was not investigated (e.g., *Tackley et al.*, 1993). *Yuen et al.* (1995) reported a non-equilibrium Ra-Nu scaling that deviated from the $1/3$ power-law exponent in the time immediately after a single avalanche event, although they attributed these deviations to core cooling or time-decaying radiogenic heating, which is not a feature in any of the models presented in this study. *Christensen and Yuen* (1985) reported that a decrease in the phase buoyancy parameter of an endothermic transition can cross a critical threshold after which the Nusselt number increases in a stepwise manner. They reported that this critical phase buoyancy is smaller (i.e., lower magnitude but still negative) for increasingly higher Rayleigh numbers. In the WMF system studied here, however, the combined phase and thermal buoyancy of the WMF transition does not appear to weaken at the higher temperatures in the "glass-ceiling" regime (S.I. Figure S20), although a full analysis of the phase fractions and complete computation of the phase buoyancy parameter Π would be needed to say for certain.

Reports of continuous high surface heat fluxes in an avalanche-dominated mantle convective systems that also appear to follow a $\beta \approx 1/3$ Rayleigh-Nusselt scaling relation have not been introduced before. It is possible they might arise in other long time-integrated models with simple parameterizations of mineral phase transitions with a low-magnitude negative Clapeyron slope (weaker than -2 MPa/K) and thus in a transitional regime (*Wolstencroft et al.*, 2009). The distinctness of the Nusselt number "jump" at higher temperatures stands out primarily in relation to the lower Nusselt numbers for mantles convecting in material with the same bulk composition of pyrolite and even within the same endothermic phase transition (WMF region), albeit a different region of it. Three-dimensional simulations of this regime are needed as the layering effects of the WMF phase transition in particular are reported to be stronger in 3D versus 2D (*Li et al.*, 2025). In our models, avalanches appear as sheet instabilities in an infinite cylinder, but *Tackley et al.* (1993) described avalanches in 3D as being cylindrically symmetric instabilities. Realistic 3D geometry of future models will affect the dynamics in the transition zone and thus affect the volume of material flushed from the MTZ and thus the surface heat flow.

The 2D simulations presented here indicate that for a complex arrangement of mineral phase transitions in $p-T$ space (or $p-S$ space), the mere presence of mantle avalanches does not necessarily indicate whether to expect a lower or higher time-averaged mantle heat flow compared to a single-layer convective system. When the layering weakens and the threshold for cold drips to avalanche is lowered, the mantle avalanches can initiate globally and continuously, overlapping in time and somewhat in space. The individual avalanche-induced "spikes" in heat flux from return flow superimpose and blur into a sustained, higher heat flux throughout the model evolution in these continuously avalanching systems.

Another way to think about the Nusselt number "jump" or "step" is that avalanches change the effective characteristic diffusion length scale of cold material at high Rayleigh number. In the absence of mantle layering, the characteristic size of a single cold drip from the convective sublayer of the stagnant lid has a high surface-area to volume ratio and would typically diffuse away into the thermal bath of the mantle before it can sink deep into the mantle. The mantle avalanche, formed from accumulating smaller cold drips into a coherent downwelling, has a much smaller surface-area to volume ratio and correspondingly larger diffusive length-scales. Therefore, the avalanche can more effectively transport cold material from near the surface and place deeper into the interior. This efficiency reasoning is akin to why mobile-lid/plate-tectonic systems have more efficient planetary cooling compared to pure stagnant lid systems. These "equilibrium avalanche" regimes are more similar to mobile lid regimes in how they can rapidly place sizable amounts of cold material deep enough into the interior to drive stronger planetary cooling.

An "equilibrium avalanche" description can explain the velocity scaling in Figure 11b: avalanches and their return flows are faster than the rate of material advection via thermal buoyancy forces (i.e., the convective velocity) and are therefore more efficiently transporting heat. They are coherent structures composed of the smaller scale drip instabilities that only become coherent due to the effect of phase transitions. Other sub-fields of fluid dynamics have shown that pulsating, reciprocal flow (i.e., a washing back and forth motion, like avalanches with return flow) may be a more efficient mechanism for heat transfer than smooth, unidirectional laminar flow (*Ye et al.*, 2021). The heat transfer enhancement effect of pulsating flow is utilized in aerospace engineering, mechanical engineering, agriculture, and many other fields, yet the precise mechanism remains poorly understood (*Ye et al.*, 2021). Further work on the time behavior of mantle avalanches (e.g., *Herein et al.*, 2013) and their ability to enhance heat flow as a specific planform of large-scale circulation (*Richter*, 1973) at different spatiotemporal frequencies may be an interesting future direction in theoretical mantle convection research.

5.3 Insights on time evolution, temperature evolution, and energy flow

Without running 3D models that are designed to be transient– with decaying internal and basal heat sources– it is difficult to precisely determine how long a "glass-ceiling" regime might last in the thermal evolution of a planet. In this sub-section, we will use our quasi-steady state results to speculate what the effects of a complex arrangement of mineral phase transitions may be on transient mantle convection.

Because our convection models are compressible and include the effects of a realistic array of many overlapping endothermic and exothermic mineral phase transitions, the relationship between the temperature and the energy budget of the mantle system is more complex than in an incompressible, Boussinesq model. In the steady state ($dE_{\text{internal}}/dt \approx 0$) for an incompressible Boussinesq model with an insulated bottom boundary and a constant rate of radiogenic heating, surface heat flow out should equal the constant rate of heat production within (e.g., *Daly*, 1980). In fully compressible mantle convection models with realistic mineral phase transitions, the energy budget is more involved. Energy terms are associated not only with changes in the internal temperature, but also with adiabatic expansion and compression as well as the release or consumption of heat at phase transitions. Figure 14 shows a summary of all eighteen models in our study in terms of their changing internal thermal energy and temperature after the plume-merging stage. Some models increase in temperature along with increases to their internal thermal energy, while others decrease in temperature with similar increases in internal energy (see $1900\,\mathrm{K}$ $\Delta\eta_{\text{ref}} = 100$ versus $\Delta\eta_{\text{ref}} = 30$). The $1700\,\mathrm{K}$ internally-heated model increases in temperature even when the internal thermal energy of the model decreases. These different pathways away from the origin represent different responses of the models to energy input, changing specific heat capacity, endo- and exothermic phase transitions occurring at constant entropy, and mantle compressibility effects. These plots show how thermal energy in these mantle models exists in different forms: contributing to higher temperatures, stored/released at phase transitions, and from the compression/expansion of material. The entropy-pressure state of the mantle determines the stable phases and their transitions which in turn affect the dynamics of the convection, which then effect the efficacy of heat flow through the mantle, across the CMB and the lithosphere which then affects the rate of planetary cooling. One could imagine a state somewhere between the $1700\,\mathrm{K}$ bottom heated and internally heated models (Fig. 14) where energy is leaving the system through the surface, but the internal temperature increases. This stable state may be close enough to the WMF region that some layering and secondary plumes might occur in 3D models where layering has been shown to be stronger at lower temperatures (*Li et al.*, 2025).

In a truly transient cooling model, the evolution "angle" on axes like Fig. 14 might be different due to hysteresis effects: directional dependence in the coupled effects of mantle temperature on phase transitions, dynamics, and overall energy budget. Future modeling studies on such transient evolutions are necessary in order to determine how a planet like Venus, for example, could evolve from some initial condition into a "glass-ceiling" regime, especially under the conditions of significant mantle melting and resurfacing that are needed to explain Venus' present day cratering record. The final subsection of this section will discuss implication for Venus further.

5.4 Implications for Venus

The high-efficiency stagnant lid convective regime identified here could provide a solution to some of the apparently contradictory constraints regarding Venus' present-day energy budget. Analysis of gravity and topography data for ≈ 10 large (1000–2000 km diam) volcanic rises imply the presence of mantle plumes rising from the core mantle boundary (e.g., *Smrekar and Phillips*, 1991; *Stofan and Smrekar*, 2005), which requires core heat loss. The absence of a dynamo has also been interpreted to indicate limits on core heat flow and recent mobile lid convection (*Nimmo*, 2002; *King*, 2018). Alternatively, compositional stratification could also affect core convection and dynamo generation (*Jacobson et al.*, 2017). The absence of current plate tectonics on Venus implies a stagnant, or at least low mobility lid regime. Early models of stagnant lid convection imply a thick thermal boundary layer and low surface heat flow. However Venus' Earth-like concentration of radiogenic isotopes (*Surkov et al.*, 1984, 1986) is inconsistent with low heat flow through out its evolution, leading some to propose that Venus cycles between stagnant and mobile states, punctuated by episodic overturn of the lithosphere (*Turcotte*, 1993; *Strom et al.*, 1994; *Armann and Tackley*, 2012; *Weller and Kiefer*, 2020), with low heat flow predicted for the current stagnant lid. This catastrophic overturn hypothesis, however, is not supported by Venus' center of mass to center of figure offset (*King*, 2018) which posits that hemispherical heterogeneity in mantle density due to a large overturn would be detectable in the offset between Venus' center of mass and geodetic center.

The emerging view of Venus as a planet with both locally high heat flow and active volcanism is a further challenge to classic stagnant lid models. Surface heat flow can be estimated in regions where the elastic lithosphere exhibits bending under a load, and by analyzing gravity and topography in the spectral domain to determine the wavelength of flexure and thus the elastic thickness. *Smrekar et al.* (2023, 2025) estimate elastic thickness from topographic flexure for 89 coronae (possible small-scale plumes) and rift flanks, folding in estimates from prior studies. They use elastic thickness to estimate heat flow, which can in turn be used to estimate thermal lithospheric thickness. Given that many of these features are likely to have active, small-scale plumes, rifting and volcanism, they are skewed toward high heat flow and thin lithosphere relative to other regions on Venus. Independent lines of evidence for active or recent volcanism in these regions (e.g., *Smrekar et al.*, 2010; *Brossier et al.*, 2020; *Herrick and Hensley*, 2023) corroborate this result. Although the low-resolution Magellan gravity field results in very large error bars (at least ± 10 km) on elastic thickness derived from admittance (*Anderson and Smrekar*, 2006), the elastic thickness estimates derived from this approach are in good agreement with values from flexure (*Smrekar et al.*, 2023, 2025). This near-global map shows finds approximately roughly 40% of the planet has thin (5–25 km) and another 40% has thick (25–55km) elastic lithosphere, accounting for known model biases. *Anderson and Smrekar* (2006) were unable to find a fit to the data in the remaining 20% of the planet due to insufficient resolution. Assuming a constant thermal conductivity of $3\mathrm{W}/(\mathrm{mK})$ and linear thermal gradient, this range of elastic thickness translates into a thermal lithospheric thickness range of 50–200 km, as defined by the depth to a temperature of $1300°\mathrm{C}$.

Maia et al. (2025) investigate a similar question of the seismogenic thickness, linked to the mechanical thickness, of Venus. In addition to incorporating prior elastic thickness estimates, they also consider global thermal evolution models with varying ratios of extrusive and intrusive volcanism and upper mantle temperature variations from gravity and topography analyses. For their nominal model, they choose lower temperature isotherms to define seismogenic and thermal lithospheric thickness ($600°\mathrm{C}$ and $1127°\mathrm{C}$) than *Smrekar et al.* (2023, 2025), who use $740°\mathrm{C}$ and $1300°\mathrm{C}$. As a result, they favor a somewhat smaller range of values of 2–35 km for seismogenic thickness. As both *Maia et al.* (2025) and *Smrekar et al.* (2023, 2025) note, depending on assumptions including strain rate, rheology/crustal thickness, and thermal conductivity, the resulting mechanical/seismogenic thickness estimates will vary somewhat. The key constraint is the presence of significant variations in mechanical thickness, heat flow, and the resulting thermal lithospheric thickness (typically 2–4 times larger than elastic or mechanical lithospheric thickness). These variations likely imply a combination of processes, including both intrusive volcanism above to small scale plumes and rifts and lithospheric thickening due to downwellings.

The "glass-ceiling" mode of convection is defined by a continuous state of mantle avalanches formed from the conglomeration of drip instabilities from the base of a dominantly stagnant lithosphere. With regard to the reasoning presented in *King* (2018), a "glass-ceiling" regime might not register as a center-of-mass/center-of-figure offset if the avalanche distribution is roughly symmetric around the mantle; however, full 3D models would need to be examined to explore this explanation as well as to determine the 3D shape of such mantle downwellings. The lack of Venus' magnetic field despite strong evidence of long-wavelength dynamically-supported features is an outstanding problem in Venus research. Based on our models, the observed lack of magnetic field on Venus can be interpreted as Venus' core simply remaining in a sub-adiabatic state, even when subjected to the sharp temperature contrast of mantle avalanches. Discussions about our models' core heat flow compared to Venus' are complicated by the fact

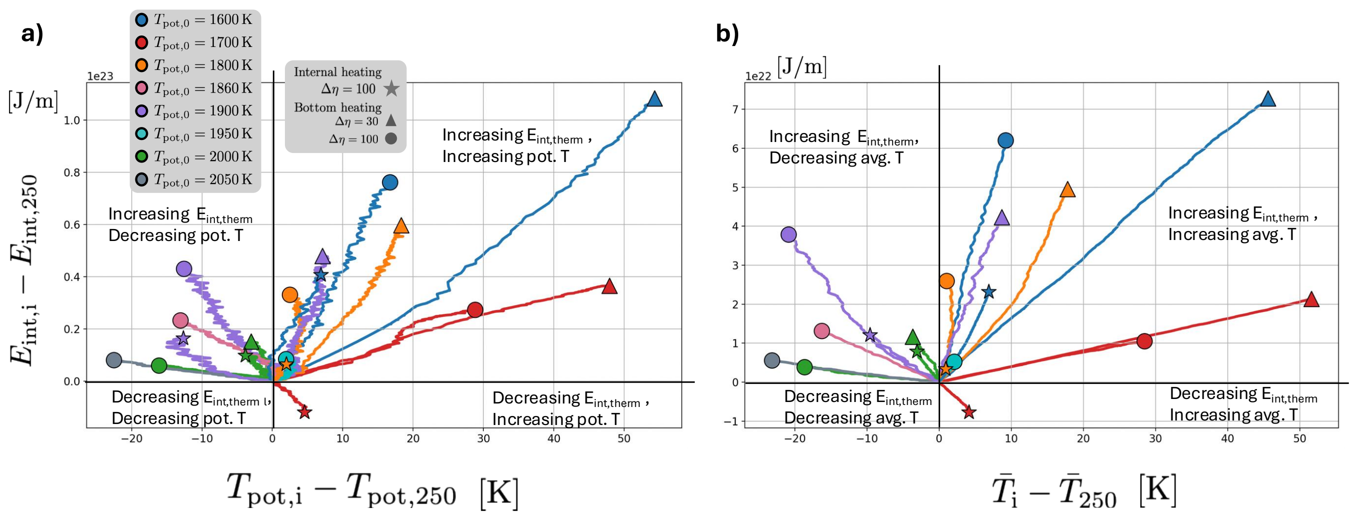

temperature changes
compression/expansion
endothermic + exothermic transitions

$$\frac{dE_{\mathrm{int,therm.}}}{dt} = Q_{\mathrm{boundary}} + Q_{\mathrm{radiogenic}} + Q_{\mathrm{shear}}$$

FIGURE 14 – These plots show how temperature changes over the course of the model evolution track with changes in internal energy (known sources minus known sinks). The origin of the coordinate axes represents the temperature/energy state at a reference time 250 time-steps into the model evolution, past the transient stage. Plot (a) examines the lower mantle potential temperature changes and (b) examines changes to the volumetrically averaged temperature throughout the domain. The equation at the bottom demonstrates the components being registered as internal energy change: changes in temperature, compression/expansion, and latent heat release/consumption.

that the surface area of Venus' core is about one fourth that of Venus' surface whereas our 2D models assume that ratio is about one half. In addition, the surface area of the MTZ— which releases and consumes heat at varying magnitudes and polarity for different sequences of mineral phase transitions— adds another aspect to energy budget accounting in 2D versus 3D and our trying to constrain the true heat flux across Venus' CMB.

The spherically integrated conductive surface heat flows from the numerical models in this study (and corrected using the temperature gradient errors reported for 2D cylindrical geometry by *Fleury et al.*, 2024) are estimated to be $\approx 13.6 - 17.3$ TW for a planet with T_m above $1950\,\mathrm{K}$. This is in contrast to heat flows of ≈ 10 TW at or around $T_m \approx 1900$ K or heat flows $\approx$ 7 TW at and around $T_m \approx 1800$ K (see Table3). The variabilities of the surface heat fluxes in our models also experience a transition, as evidenced in Figure 6b in the absence of core heating. Perhaps the higher heat flows (as evidenced by the higher Nusselt numbers) in our "glass-ceiling" numerical models are consistent with regions of Venus exhibiting Earth-like heat flow, despite lacking plate tectonics.

The surface heat flux profiles in our "glass-ceiling" models (Figure 6c,d) are consistent with high frequency local variations in lithosphere thickness which induces a similarly high-frequency pattern of surface heat flux. The base of Venus' lithosphere may be undergoing small scale convection in which drips persistently layer at the MTZ before their combined weight drive frequent, global mantle avalanches to replenish the upper mantle with hot material and drive more small scale convection in the lower lithosphere. Further analysis of the gravity and dynamic topography signature (e.g., *Kerr et al.*, 2025) of small-scale convection and avalanches occurring below the stagnant or "squishy" (*Lourenço et al.*, 2020) lid of Venus is a necessary area of future work.

Intrusive volcanism, thinner lithosphere, and melting all invariably play a role in explaining Venus' global array of multi-scale volcanic features. While intrusive magmatism on its own does not speak to the plume-thermal dichotomy on Venus, the effects of volcanism and phase transitions likely work in concert. The latent heat of crystallization released upon the partial melting of pyrolitic mantle can heat the mantle locally and change its composition by partitioning melt-compatible elements into the fluid phase. The melt can be released as intrusive or extrusive volcanism which can weaken the lithosphere and/or resurface it locally, respectively. Changes in composition post-melting likely have important dynamical effects as well. Particularly, the partial melt products of pyrolite (basalt and harzburgite) have different stability regions in p-T space for the majoritic garnet phase of interest (*Faccenda and Dal Zilio*, 2017). A future model that deals with the energetic and compositional changes due to melting may be able to disentangle the effects of melting and mantle dynamics in the upper mantle and MTZ on Venus' surface heat flow. The model in this study will provide a useful baseline for future modeling efforts as these additional processes are accounted for. Lastly, it is possible that multiple types of mineral phase transitions (e.g., the ringwoodite to bridgmanite reaction as described in *Steinbach and Yuen*, 1992) may also play a role in mantle layering. The mineral physics look-up table for pyrolite is different than that of basalt, harzburgite, and even a mechanical mixture of the two compositions. Each may play complementary or competing roles in explaining the distribution and scale of Venus' plume-driven features, the sources of global magmatism and crustal growth on Venus, and its sparse and approximately uniformly distributed cratering record.

One-dimensional parameterized convection is still a useful tool in thermal evolution models for planets like Venus and Earth. In Figures 8, 9, and 10 we have included the pre-factor a in equations 13 and 15 that correspond to $\beta = 1/3$ power law functions passing through the final timestep of the 1800K-100x model and that of the 2000K-100x model. The proportional relationship of these pre-factors (26% for Ra vs. Nu and 38% for Ra/θ vs. $\mathrm{Nu}\theta$) could be implemented in such a parameterized convection model. For a planet with stagnant lid tectonics, for example, a heat pipe tectonic regime may be relevant for the hottest stage of a planet's evolution. Below the solidus, a "glass-ceiling" regime may take effect with a higher pre-factor a. Then, after a certain critical temperature (~ 1900 K) is passed, this pre-factor can be adjusted to a lower value consistent with the classical boundary-layer theory parameterization of the convection.

6 Conclusions

Exploring how mineral phase changes facilitate a deviation from an expected Rayleigh-Nusselt scaling into a state of higher efficiency cooling at higher temperatures is an important aspect of better understanding terrestrial cooling evolutions for Earth, Venus, and other Earth-like exoplanets. Decades of research has been devoted to understanding thermal convection in a stagnant lid system and how simply parameterized endothermic and exothermic phase transitions can layer mantle flow and release it suddenly as mantle avalanches. As mantle convection models become more complex, understanding how realistic, overlapping mineral phases affect mantle dynamics and heat flow will become increasingly important. Improvements in understanding the effects of mineral phase transitions may help to resolve long-standing geodynamics questions about the thermal history of Earth, as many 1D thermal evolution models use simple Rayleigh-Nusselt scaling parameterizations with constant Ra-Nu scaling parameters (a & β, equation (14)) to describe the dynamics of the convecting mantle throughout history (e.g., *Christensen*, 1985). These 1D models can be improved by considering the inhibiting and/or enhancing effects of mineral phase transitions on mantle flow and surface heat flux throughout Earth's history and perhaps help us to understand the ways Venus may have evolved differently than Earth.

The results of this study show that in a stagnant lid planet with a bulk pyrolite mantle, between potential temperatures of $1900\text{-}2000\ \mathrm{K}$, the mantle transitions to a regime of continuous mantle avalanches which, somewhat counterintuitively, increases the efficiency of heat flow. This increased-efficiency regime is surprisingly long-lasting compared to the transient spikes in heat flow examined in previous studies of mantle avalanches and appears to follow a $\beta = 1/3$ Ra-Nu scaling trend. This unexpectedly high heat flow regime in a planet without plate tectonics may be relevant for Venus, which lacks plate tectonics but possesses many characteristics of a volcanically and tectonically active planet including variable and locally high heat flow.

Acknowledgements

This material is based upon work supported by the U.S. Department of Energy, Office of Science, Office of Advanced Scientific Computing Research, Department of Energy Computational Science Graduate Fellowship under Award Number DESC0022158. The authors are thankful for support from NASA Award 80NSSC22K0100. Computational resources were provided by Extreme Science and Engineering Discovery Environment (XSEDE), which is supported by National Science Foundation grant number ACI-1053575. This research used resources of the National Energy Research Scientific Computing Center (NERSC), a Department of Energy Office of Science User Facility using NERSC award ASCRERCAP0026889. This research was partially conducted at the Jet Propulsion Laboratory, California Institute of Technology, under contract (80NM0020F0035) with the National Aeronautics and Space Administration. This research was partially conducted at the Jet Propulsion Laboratory, California Institute of Technology, under contract 80NM0018D0004 with the National Aeronautics and Space Administration. We acknowledge the use of imagery from Venus QuickMap (https://venus.quickmap.io), a collaboration between NASA GSFC& Applied Coherent Technology Corp. We thank the Computational Infrastructure for Geodynamics (geodynamics.org) which is funded by the National Science Foundation under award EAR-0949446 and EAR-1550901 for supporting the development of ASPECT. The authors are also grateful for dicussions with Carolina Lithgow-Bertelloni and her group at UCLA as well as the thoughtful reviews .

Author contributions

Conceptualization [MCK, DRS, SES]
Formal analysis [MCK]
Funding acquisition [MCK, DRS, SES]
Investigation [MCK]
Methodology [MCK, DRS]
Project administration [MCK, DRS]
Resources [MCK, DRS]
Software [MCK]
Supervision [MCK, DRS, SES]
Validation [MCK]
Visualization [MCK]
Writing – original draft [MCK, DRS, SES]
Writing – review & editing [MCK, DRS, SES]

Data availability

The parameter files used in this study for ASPECT version 2.4 can be found in the following Zenodo repository along with data tables of post-processed model output as well as the Python modules and scripts used to conduct the analysis and make the figures: https://doi.org/10.5281/zenodo.18520532.

Competing interests

Declare any competing interests.

Copyright notice

References

Adams, A. C., D. R. Stegman, H. Mohammadzadeh, S. E. Smrekar, and P. J. Tackley (2023), Plume-Induced Delamination Initiated at Rift Zones on Venus, *Journal of Geophysical Research: Planets*, *128*(10), e2023JE007,879, doi: http://doi.org/10.1029/2023JE007879.

Anderson, F. S., and S. E. Smrekar (2006), Global mapping of crustal and lithospheric thickness on Venus, *Journal of Geophysical Research: Planets*, *111*(E8), 2004JE002,395, doi: http://doi.org/10.1029/2004JE002395.

Armann, M., and P. J. Tackley (2012), Simulating the thermochemical magmatic and tectonic evolution of Venus's mantle and lithosphere: Two-dimensional models, *Journal of Geophysical Research: Planets*, *117*(E12), 2012JE004,231, doi: http://doi.org/10.1029/2012JE004231.

Auerbach, V., and D. R. Stegman (2025), Thermal Evolution of Planetary Interiors With a Crystallizing Basal Magma Ocean Coupled to Parameterized Mantle Convection, *Journal of Geophysical Research: Planets*, *130*(7), e2025JE009,016, doi: http://doi.org/10.1029/2025JE009016.

Bangerth, W., J. Dannberg, M. Fraters, R. Gassmoeller, A. Glerum, T. Heister, R. Myhill, and J. Naliboff (2022), ASPECT v2.4.0, doi: http://doi.org/10.5281/ZENODO.6903424.

Bercovici, D., G. Schubert, G. A. Glatzmaier, and A. Zebib (1989), Three-dimensional thermal convection in a spherical shell, *Journal of Fluid Mechanics*, *206*, 75–104, doi: http://doi.org/10.1017/S0022112089002235.

Brossier, J. F., M. S. Gilmore, and K. Toner (2020), Low radar emissivity signatures on Venus volcanoes and coronae: New insights on relative composition and age, *Icarus*, *343*, 113,693, doi: http://doi.org/10.1016/j.icarus.2020.113693.

Bunge, H.-P., M. A. Richards, and J. R. Baumgardner (1997), A sensitivity study of three-dimensional spherical mantle convection at 10^8 Rayleigh number: Effects of depth-dependent viscosity, heating mode, and an endothermic phase change, *Journal of Geophysical Research: Solid Earth*, *102*(B6), 11,991–12,007, doi: http://doi.org/10.1029/96JB03806.

Butler, S. L., and W. R. Peltier (2000), On scaling relations in time-dependent mantle convection and the heat transfer constraint on layering, *Journal of Geophysical Research: Solid Earth*, *105*(B2), 3175–3208, doi: http://doi.org/10.1029/1999JB900377.

Christensen, U. R. (1984), Heat transport by variable viscosity convection and implications for the Earth's thermal evolution, *Physics of the Earth and Planetary Interiors*, *35*(4), 264–282, doi: http://doi.org/10.1016/0031-9201(84)90021-9.

Christensen, U. R. (1985), Thermal evolution models for the Earth, *Journal of Geophysical Research: Solid Earth*, *90*(B4), 2995–3007, doi: http://doi.org/10.1029/JB090iB04p02995.

Christensen, U. R., and D. A. Yuen (1984), The interaction of a subducting lithospheric slab with a chemical or phase boundary, *Journal of Geophysical Research: Solid Earth*, *89*(B6), 4389–4402, doi: http://doi.org/10.1029/JB089iB06p04389.

Christensen, U. R., and D. A. Yuen (1985), Layered convection induced by phase transitions, *Journal of Geophysical Research: Solid Earth*, *90*(B12), 10,291–10,300, doi: http://doi.org/10.1029/JB090iB12p10291.

Condie, K. C. (1998), Episodic continental growth and supercontinents: a mantle avalanche connection?, *Earth and Planetary Science Letters*, *163*(1-4), 97–108, doi: http://doi.org/10.1016/S0012-821X(98)00178-2.

Courtillot, V., A. Davaille, J. Besse, and J. Stock (2003), Three distinct types of hotspots in the Earth's mantle, *Earth and Planetary Science Letters*, *205*(3-4), 295–308, doi: http://doi.org/10.1016/S0012-821X(02)01048-8.

Daly, S. F. (1980), Convection with decaying heat sources: constant viscosity, *Geophysical Journal International*, *61*(3), 519–547, doi: http://doi.org/https://doi.org/10.1111/j.1365-246X.1980.tb04831.x.

Dannberg, J., R. Gassmöller, R. Li, C. Lithgow-Bertelloni, and L. Stixrude (2022), An entropy method for geodynamic modelling of phase transitions: capturing sharp and broad transitions in a multiphase assemblage, *Geophysical Journal International*, *231*(3), 1833–1849, doi: http://doi.org/10.1093/gji/ggac293.

Davaille, A., and C. Jaupart (1993), Transient high-Rayleigh-number thermal convection with large viscosity variations, *Journal of Fluid Mechanics*, *253*, 141–166, doi: http://doi.org/10.1017/S0022112093001740.

Deschamps, F., and C. Sotin (2001), Thermal convection in the outer shell of large icy satellites, *Journal of Geophysical Research: Planets*, *106*(E3), 5107–5121, doi: http://doi.org/10.1029/2000JE001253.

Dubuffet, F., M. Rabinowicz, and M. Monnereau (2000), Multiple scales in mantle convection, *Earth and Planetary Science Letters*, *178*(3-4), 351–366, doi: http://doi.org/10.1016/S0012-821X(00)00081-9.

Eide, E. A., and T. H. Torsvik (1996), Paleozoic supercontinental assembly, mantle flushing, and genesis of the Kiaman Superchron, *Earth and Planetary Science Letters*, *144*(3-4), 389–402, doi: http://doi.org/10.1016/S0012-821X(96)00176-8.

Faccenda, M., and L. Dal Zilio (2017), The role of solid–solid phase transitions in mantle convection, *Lithos*, *268-271*, 198–224, doi: http://doi.org/10.1016/j.lithos.2016.11.007.

Fleury, A., A.-C. Plesa, C. Hüttig, and D. Breuer (2024), Assessing the Accuracy of 2-D Planetary Evolution Models Against the 3-D Sphere, *Geochemistry, Geophysics, Geosystems*, *25*(2), e2023GC011,114, doi: http://doi.org/10.1029/2023GC011114.

Frank-Kamenetskii, D. A. (2015), *Diffusion and Heat Exchange in Chemical Kinetics*, Princeton University Press, Princeton, NJ, doi: http://doi.org/10.1515/9781400877195.

Garrido-Tomasini, J., A. Lenardic, W. Moore, and M. Weller (2025), Infinite Prandtl number, mixed-heated convection in a spherical domain: velocity and heat flux scaling trends, *Geophysical Journal International*, *241*(1), 203–218, doi: http://doi.org/10.1093/gji/ggaf039.

Gassmöller, R., J. Dannberg, W. Bangerth, T. Heister, and R. Myhill (2020), On formulations of compressible mantle convection, *Geophysical Journal International*, *221*(2), 1264–1280, doi: http://doi.org/10.1093/gji/ggaa078.

Giannandrea, E., and U. Christensen (1993), Variable viscosity convection experiments with a stress-free upper boundary and implications for the heat transport in the Earth's mantle, *Physics of the Earth and Planetary Interiors*, *78*(1-2), 139–152, doi: http://doi.org/10.1016/0031-9201(93)90090-V.

Grasset, O., and E. M. Parmentier (1998), Thermal convection in a volumetrically heated, infinite Prandtl number fluid with strongly temperature-dependent viscosity: Implications for planetary thermal evolution, *Journal of Geophysical Research: Solid Earth*, *103*(B8), 18,171–18,181, doi: http://doi.org/10.1029/98JB01492.

Grigné, C. (2023), Stagnant-lid convection: comparison of viscosity laws and uniform scaling approach for temperature and heat flux prediction, *Geophysical Journal International*, *235*(3), 2410–2429, doi: http://doi.org/10.1093/gji/ggad375.

Gurnis, M. (1989), A reassessment of the heat transport by variable viscosity convection with plates and lids, *Geophysical Research Letters*, *16*(2), 179–182, doi: http://doi.org/10.1029/GL016i002p00179.

Gülcher, A. J. P., L. Sabbeth, E. Stofan, and S. E. Smrekar (2025), Coronae on Venus: An Updated Global Database and Insights Into Morphology, Spatial Distribution, Geological Setting, and Lithospheric Properties, *Journal of Geophysical Research: Planets*, *130*(5), e2024JE008,749, doi: http://doi.org/10.1029/2024JE008749.

Hansen, U., and A. Ebel (1984), Experiments with a numerical model related to mantle convection: boundary layer behaviour of small- and large scale flows, *Physics of the Earth and Planetary Interiors*, *36*(3-4), 374–390, doi: http://doi.org/10.1016/0031-9201(84)90058-X.

Heister, T., J. Dannberg, R. Gassmöller, and W. Bangerth (2017), High accuracy mantle convection simulation through modern numerical methods – II: realistic models and problems, *Geophysical Journal International*, *210*(2), 833–851, doi: http://doi.org/10.1093/gji/ggx195.

Herein, M., A. Galsa, and L. Lenkey (2013), Impact of the Rayleigh number and endothermic phase transition on the time behaviour of mantle avalanches, *Journal of Geodynamics*, *66*, 103–113, doi: http://doi.org/10.1016/j.jog.2013.02.007.

Herrick, R. R., and S. Hensley (2023), Surface changes observed on a Venusian volcano during the Magellan mission, *Science*, *379*(6638), 1205–1208, doi: http://doi.org/10.1126/science.abm7735.

Honda, S., D. A. Yuen, S. Balachandar, and D. Reuteler (1993), Three-Dimensional Instabilities of Mantle Convection with Multiple Phase Transitions, *Science*, *259*(5099), 1308–1311, doi: http://doi.org/10.1126/science.259.5099.1308.

Iwase, Y., and S. Honda (1997), An interpretation of the Nusselt-Rayleigh number relationship for convection in a spherical shell, *Geophysical Journal International*, *130*(3), 801–804, doi: http://doi.org/10.1111/j.1365-246X.1997.tb01874.x.

Jacobson, S. A., D. C. Rubie, J. Hernlund, A. Morbidelli, and M. Nakajima (2017), Formation, stratification, and mixing of the cores of Earth and Venus, *Earth and Planetary Science Letters*, *474*, 375–386, doi: http://doi.org/10.1016/j.epsl.2017.06.023.

Jellinek, A. M., and A. Lenardic (2009), Effects of spatially varying roof cooling on thermal convection at high Rayleigh number in a fluid with a strongly temperature-dependent viscosity, *Journal of Fluid Mechanics*, *629*, 109–137, doi: http://doi.org/10.1017/S0022112009006260.

Jimenez, J., and J. A. Zufiria (1987), A boundary-layer analysis of Rayleigh-Bénard convection at large Rayleigh number, *Journal of Fluid Mechanics*, *178*, 53–71, doi: http://doi.org/10.1017/S0022112087001113.

Kerr, M. C., and D. R. Stegman (2024), Mantle avalanches in a Venus-like stagnant lid planet, *Earth and Planetary Physics*, *8*(5), 686–702, doi: http://doi.org/10.26464/epp2024062.

Kerr, M. C., D. R. Stegman, S. E. Smrekar, and A. C. Adams (2025), The glass-ceiling convective regime and the origin and diversity of coronae on Venus, *Proceedings of the National Academy of Sciences*, *122*(38), e2504491,122, doi: http://doi.org/10.1073/pnas.2504491122.

King, S. D. (2018), Venus Resurfacing Constrained by Geoid and Topography, *Journal of Geophysical Research: Planets*, *123*(5), 1041–1060, doi: http://doi.org/10.1002/2017JE005475.

King, S. D., D. J. Frost, and D. C. Rubie (2015), Why cold slabs stagnate in the transition zone, *Geology*, *43*(3), 231–234, doi: http://doi.org/10.1130/G36320.1.

Koch, D. M. (1994), A spreading drop model for plumes on Venus, *Journal of Geophysical Research: Planets*, *99*(E1), 2035–2052, doi: http://doi.org/10.1029/93JE03097.

Korenaga, J., and T. H. Jordan (2003), Physics of multiscale convection in Earth's mantle: Onset of sublithospheric convection, *Journal of Geophysical Research: Solid Earth*, *108*(B7), 2002JB001,760, doi: http://doi.org/10.1029/2002JB001760.

Kronbichler, M., T. Heister, and W. Bangerth (2012), High accuracy mantle convection simulation through modern numerical methods: High accuracy mantle convection simulation, *Geophysical Journal International*, *191*(1), 12–29, doi: http://doi.org/10.1111/j.1365-246X.2012.05609.x.

Li, R., J. Dannberg, R. Gassmöller, C. Lithgow-Bertelloni, and L. Stixrude (2025), How Phase Transitions Impact Changes in Mantle Convection Style Throughout Earth's History: From Stalled Plumes to Surface Dynamics, *Geochemistry, Geophysics, Geosystems*, *26*(2), e2024GC011,600, doi: http://doi.org/10.1029/2024GC011600.

Liu, M., D. A. Yuen, W. Zhao, and S. Honda (1991), Development of Diapiric Structures in the Upper Mantle Due to Phase Transitions, *Science*, *252*(5014), 1836–1839, doi: http://doi.org/10.1126/science.252.5014.1836.

Lourenço, D. L., A. B. Rozel, M. D. Ballmer, and P. J. Tackley (2020), Plutonic-Squishy Lid: A New Global Tectonic Regime Generated by Intrusive Magmatism on Earth-Like Planets, *Geochemistry, Geophysics, Geosystems*, *21*(4), e2019GC008,756, doi: http://doi.org/10.1029/2019GC008756.

Machetel, P., and E. Thomassot (2002), Cretaceous length of day perturbation by mantle avalanche, *Earth and Planetary Science Letters*, *202*(2), 379–386, doi: http://doi.org/10.1016/S0012-821X(02)00785-9.

Machetel, P., and P. Weber (1991), Intermittent layered convection in a model mantle with an endothermic phase change at 670 km, *Nature*, *350*(6313), 55–57, doi: http://doi.org/10.1038/350055a0.

Maia, J. S., A.-C. Plesa, I. Van Zelst, R. Ghail, A. J. Gülcher, M. P. Panning, S. P. Näsholm, B. De Toffoli, A. C. Horleston, K. T. Smolinski, et al. (2025), The seismogenic thickness of Venus, *Journal of Geophysical Research: Planets*, *130*(7), e2025JE009,065, doi: http://doi.org/10.1029/2025JE009065.

Malkus, W. V. R. (1954), The heat transport and spectrum of thermal turbulence, *Proceedings of the Royal Society of London. Series A. Mathematical and Physical Sciences*, *225*(1161), 196–212, doi: http://doi.org/10.1098/rspa.1954.0197.

Manga, M., and D. Weeraratne (1999), Experimental study of non-Boussinesq Rayleigh–Bénard convection at high Rayleigh and Prandtl numbers, *Physics of FLUIDS*, *11*(10), 2969–2976, doi: http://doi.org/10.1063/1.870156.

Michaut, C., A. Davaille, and S. Labrosse (2025), Formation and Evolution of Planetary Stagnant Lids and Crusts, *Annual Review of Fluid Mechanics*, doi: http://doi.org/10.1146/annurev-fluid-112723-055048.

Moore, W. B. (2008), Heat transport in a convecting layer heated from within and below, *Journal of Geophysical Research: Solid Earth*, *113*(B11), doi: http://doi.org/10.1029/2006JB004778.

Nimmo, F. (2002), Why does Venus lack a magnetic field?, *Geology*, *30*(11), 987–990, doi: http://doi.org/10.1130/0091-7613(2002)030<0987:WDVLAM>2.0.CO;2.

Olson, P. (1987), A comparison of heat transfer laws for mantle convection at very high Rayleigh numbers, *Physics of the Earth and Planetary Interiors*, *48*(1-2), 153–160, doi: http://doi.org/10.1016/0031-9201(87)90118-X.

Olson, P., and D. A. Yuen (1982), Thermochemical plumes and mantle phase transitions, *Journal of Geophysical Research: Solid Earth*, *87*(B5), 3993–4002, doi: http://doi.org/10.1029/JB087iB05p03993.

O'Neill, C. (2020), Planetary thermal evolution models with tectonic transitions, *Planetary and Space Science*, *192*, 105,059, doi: http://doi.org/10.1016/j.pss.2020.105059.

Peltier, W. R., and L. P. Solheim (1992a), Mantle phase transitions and layered chaotic convection, *Geophysical Research Letters*, *19*(3), 321–324, doi: http://doi.org/10.1029/91GL02951.

Peltier, W. R., and L. P. Solheim (1992b), Mantle Phase Transitions, Layered Chaotic Convection, and the Viscosity of the Deep Mantle, in *Chaotic Processes in the Geological Sciences*, vol. 41, edited by A. Friedman, W. Miller, and D. A. Yuen, pp. 111–139, Springer US, New York, NY, doi: http://doi.org/10.1007/978-1-4684-0643-6$_6$, series title: The IMA Volumes in Mathematics and its Applications.

Priestley, C. H. B. (1954), Convection from a large horizontal surface, *Australian Journal of Physics*, *7*(1), 176–201, doi: http://doi.org/10.1071/PH540176.

Ratcliff, J. T., G. Schubert, and A. Zebib (1996), Steady tetrahedral and cubic patterns of spherical shell convection with temperature-dependent viscosity, *Journal of Geophysical Research: Solid Earth*, *101*(B11), 25,473–25,484, doi: http://doi.org/10.1029/96JB02097.

Reese, C., V. Solomatov, and L.-N. Moresi (1999), Non-Newtonian Stagnant Lid Convection and Magmatic Resur facing on Venus, *Icarus*, *139*(1), 67–80, doi: http://doi.org/10.1006/icar.1999.6088.

Reese, C. C., V. S. Solomatov, and J. R. Baumgardner (2005), Scaling laws for time-dependent stagnant lid convection in a spherical shell, *Physics of the Earth and Planetary Interiors*, *149*(3-4), 361–370, doi: http://doi.org/10.1016/j.pepi.2004.11.004.

Richter, F. M. (1973), Convection and the large-scale circulation of the mantle, *Journal of Geophysical Research*, *78*(35), 8735–8745, doi: http://doi.org/10.1029/JB078i035p08735.

Richter, F. M., and D. P. McKenzie (1981), On some consequences and possible causes of layered mantle convection, *Journal of Geophysical Research: Solid Earth*, *86*(B7), 6133–6142, doi: http://doi.org/10.1029/JB086iB07p06133.

Sandwell, D. T., and G. Schubert (1992), Evidence for Retrograde Lithospheric Subduction on Venus, *Science*, *257*(5071), 766–770, doi: http://doi.org/10.1126/science.257.5071.766.

Siggia, E. D. (1994), High Rayleigh Number Convection, *Annual Review of Fluid Mechanics*, *26*(1), 137–168, doi: http://doi.org/10.1146/annurev.fl.26.010194.001033.

Smrekar, S. E., and R. J. Phillips (1991), Venusian highlands: Geoid to topography ratios and their implications, *Earth and Planetary Science Letters*, *107*(3-4), 582–597, doi: http://doi.org/10.1016/0012-821X(91)90103-O.

Smrekar, S. E., and C. Sotin (2012), Constraints on mantle plumes on Venus: Implications for volatile history, *Icarus*, *217*(2), 510–523, doi: http://doi.org/10.1016/j.icarus.2011.09.011.

Smrekar, S. E., E. R. Stofan, N. Mueller, A. Treiman, L. Elkins-Tanton, J. Helbert, G. Piccioni, and P. Drossart (2010), Recent Hotspot Volcanism on Venus from VIRTIS Emissivity Data, *Science*, *328*(5978), 605–608, doi: http://doi.org/10.1126/science.1186785.

Smrekar, S. E., C. Ostberg, and J. G. O'Rourke (2023), Earth-like lithospheric thickness and heat flow on Venus consistent with active rifting, *Nature Geoscience*, *16*(1), 13–18, doi: http://doi.org/10.1038/s41561-022-01068-0.

Smrekar, S. E., C. Ostberg, and J. G. O'Rourke (2025), Author Correction: Earth-like lithospheric thickness and heat flow on Venus consistent with active rifting, *Nature Geoscience*, *18*(1), 105–105, doi: http://doi.org/10.1038/s41561-024-01595-y.

Solheim, L., and W. Peltier (1993), Mantle phase transitions and layered convection, *Canadian Journal of Earth Sciences*, *30*(5), 881–892, doi: http://doi.org/10.1139/e93-073.

Solheim, L. P., and W. R. Peltier (1994), Avalanche effects in phase transition modulated thermal convection: A model of Earth's mantle, *Journal of Geophysical Research: Solid Earth*, *99*(B4), 6997–7018, doi: http://doi.org/10.1029/93JB02168.

Solomatov, V. S. (1995), Scaling of temperature- and stress-dependent viscosity convection, *Physics of Fluids*, *7*(2), 266–274, doi: http://doi.org/10.1063/1.868624.

Solomatov, V. S., and L. Moresi (1996), Stagnant lid convection on Venus, *Journal of Geophysical Research: Planets*, *101*(E2), 4737–4753, doi: http://doi.org/10.1029/95JE03361.

Solomatov, V. S., and L. Moresi (1997), Three regimes of mantle convection with non-Newtonian viscosity and stagnant lid convection on the terrestrial planets, *Geophysical Research Letters*, *24*(15), 1907–1910, doi: http://doi.org/10.1029/97GL01682.

Solomatov, V. S., and L. Moresi (2000), Scaling of time-dependent stagnant lid convection: Application to small-scale convection on Earth and other terrestrial planets, *Journal of Geophysical Research: Solid Earth*, *105*(B9), 21,795–21,817, doi: http://doi.org/10.1029/2000JB900197.

Steinbach, V., and D. A. Yuen (1992), The effects of multiple phase transitions on Venusian mantle convection, *Geophysical Research Letters*, *19*(22), 2243–2246, doi: http://doi.org/10.1029/92GL02319.

Steinberger, B., and A. R. Calderwood (2006), Models of large-scale viscous flow in the Earth's mantle with constraints from mineral physics and surface observations, *Geophysical Journal International*, *167*(3), 1461–1481, doi: http://doi.org/10.1111/j.1365-246X.2006.03131.x.

Stixrude, L., and C. Lithgow-Bertelloni (2005a), Thermodynamics of mantle minerals - I. Physical properties, *Geophysical Journal International*, *162*(2), 610–632, doi: http://doi.org/10.1111/j.1365-246X.2005.02642.x.

Stixrude, L., and C. Lithgow-Bertelloni (2005b), Thermodynamics of mantle minerals - I. Physical properties, *Geophysical Journal International*, *162*(2), 610–632, doi: http://doi.org/10.1111/j.1365-246X.2005.02642.x.

Stixrude, L., and C. Lithgow-Bertelloni (2011), Thermodynamics of mantle minerals - II. Phase equilibria, *Geophysical Journal International*, *184*(3), 1180–1213, doi: http://doi.org/10.1111/j.1365-246X.2010.04890.x.

Stixrude, L., and C. Lithgow-Bertelloni (2021), Thermal expansivity, heat capacity and bulk modulus of the mantle, *Geophysical Journal International*, *228*(2), 1119–1149, doi: http://doi.org/10.1093/gji/ggab394.

Stixrude, L., N. De Koker, N. Sun, M. Mookherjee, and B. B. Karki (2009), Thermodynamics of silicate liquids in the deep Earth, *Earth and Planetary Science Letters*, *278*(3-4), 226–232, doi: http://doi.org/10.1016/j.epsl.2008.12.006.

Stofan, E. R., and S. E. Smrekar (2005), Large Topographic Rises, Coronae, Large Flow Fields, and Large Volcanoes on Venus: Evidence for Mantle Plumes?, in *Plates, Plumes and Paradigms*, *Geological Society of America Special Paper*, vol. 388, edited by G. R. Foulger, J. H. Natland, D. C. Presnall, and D. L. Anderson, pp. 841–861, Geological Society of America, Boulder, Colorado, doi: http://doi.org/10.1130/0-8137-2388-4.841.

Stofan, E. R., D. L. Bindschadler, J. W. Head, and E. M. Parmentier (1991), Corona structures on Venus: Models of origin, *Journal of Geophysical Research: Planets*, *96*(E4), 20,933–20,946, doi: http://doi.org/10.1029/91JE02218.

Strom, R. G., G. G. Schaber, and D. D. Dawson (1994), The global resurfacing of Venus, *Journal of Geophysical Research: Planets*, *99*(E5), 10,899–10,926, doi: http://doi.org/10.1029/94JE00388.

Sullivan, C., and A. Kaszynski (2019), PyVista: 3D plotting and mesh analysis through a streamlined interface for the Visualization Toolkit (VTK), *Journal of Open Source Software*, *4*(37), 1450, doi: http://doi.org/10.21105/joss.01450.

Surkov, Y. A., V. Barsukov, L. Moskalyeva, V. Kharyukova, and A. Kemurdzhian (1984), New data on the composition, structure, and properties of Venus rock obtained by Venera 13 and Venera 14, *Journal of Geophysical Research: Solid Earth*, *89*(S02), B393–B402, doi: http://doi.org/10.1029/JB089iS02p0B393.

Surkov, Y. A., L. Moskalyova, V. Kharyukova, A. Dudin, G. Smirnov, and S. Y. Zaitseva (1986), Venus rock composition at the Vega 2 landing site, *Journal of Geophysical Research: Solid Earth*, *91*(B13), E215–E218, doi: http://doi.org/10.1029/JB091iB13p0E215.

Tackley, P. J. (1996), Effects of strongly variable viscosity on three-dimensional compressible convection in planetary mantles, *Journal of Geophysical Research: Solid Earth*, *101*(B2), 3311–3332, doi: http://doi.org/10.1029/95JB03211.

Tackley, P. J., D. J. Stevenson, G. A. Glatzmaier, and G. Schubert (1993), Effects of an endothermic phase transition at 670 km depth in a spherical model of convection in the Earth's mantle, *Nature*, *361*(6414), 699–704, doi: http://doi.org/10.1038/361699a0.

Thiriet, M., D. Breuer, C. Michaut, and A.-C. Plesa (2019), Scaling laws of convection for cooling planets in a stagnant lid regime, *Physics of the Earth and Planetary Interiors*, *286*, 138–153, doi: http://doi.org/10.1016/j.pepi.2018.11.003.

Trubitsyn, V. P., A. N. Evseev, A. A. Baranov, and A. P. Trubitsyn (2008), Influence of an endothermic phase transition on mass transfer between the upper and the lower mantle, *Izvestiya, Physics of the Solid Earth*, *44*(6), 443–455, doi: http://doi.org/10.1134/S1069351308060013.

Turcotte, D. L. (1993), An episodic hypothesis for Venusian tectonics, *Journal of Geophysical Research: Planets*, *98*(E9), 17,061–17,068, doi: http://doi.org/10.1029/93JE01775.

Turcotte, D. L., and E. R. Oxburgh (1967), Finite amplitude convective cells and continental drift, *Journal of Fluid Mechanics*, *28*(1), 29–42, doi: http://doi.org/10.1017/S0022112067001880.

Turcotte, D. L., and G. Schubert (2002), *Geodynamics*, Cambridge university press, doi: http://doi.org/10.1017/CBO9780511807442.

Weinstein, S. A. (1993), Catastrophic overturn of the Earth's mantle driven by multiple phase changes and internal heat generation, *Geophysical Research Letters*, *20*(2), 101–104, doi: http://doi.org/10.1029/93GL00044.

Weller, M. B., and W. S. Kiefer (2020), The Physics of Changing Tectonic Regimes: Implications for the Temporal Evolution of Mantle Convection and the Thermal History of Venus, *Journal of Geophysical Research: Planets*, *125*(1), e2019JE005,960, doi: http://doi.org/10.1029/2019JE005960.

Wolstencroft, M., and J. H. Davies (2011), Influence of the Ringwoodite-Perovskite transition on mantle convection in spherical geometry as a function of Clapeyron slope and Rayleigh number, *Solid Earth*, *2*(2), 315–326, doi: http://doi.org/10.5194/se-2-315-2011.

Wolstencroft, M., J. Davies, and D. Davies (2009), Nusselt–Rayleigh number scaling for spherical shell Earth mantle simulation up to a Rayleigh number of, *Physics of the Earth and Planetary Interiors*, *176*(1-2), 132–141, doi: http://doi.org/10.1016/j.pepi.2009.05.002.

Xu, W., C. Lithgow-Bertelloni, L. Stixrude, and J. Ritsema (2008), The effect of bulk composition and temperature on mantle seismic structure, *Earth and Planetary Science Letters*, *275*(1-2), 70–79, doi: http://doi.org/10.1016/j.epsl.2008.08.012.

Ye, Q., Y. Zhang, and J. Wei (2021), A comprehensive review of pulsating flow on heat transfer enhancement, *Applied Thermal Engineering*, *196*, 117,275, doi: http://doi.org/10.1016/j.applthermaleng.2021.117275.

Yuen, D., D. Reuteler, S. Balachandar, V. Steinbach, A. Malevsky, and J. Smedsmo (1994), Various influences on three-dimensional mantle convection with phase transitions, *Physics of the Earth and Planetary Interiors*, *86*(1-3), 185–203, doi: http://doi.org/10.1016/0031-9201(94)05068-6.

Yuen, D. A., S. Balachandar, V. C. Steinbach, S. Honda, D. M. Reuteler, J. J. Smedsmo, and G. S. Lauer (1995), Non-equilibrium effects of core-cooling and time-dependent internal heating on mantle flush events, *Nonlinear Processes in Geophysics*, *2*(3/4), 206–221, doi: http://doi.org/10.5194/npg-2-206-1995.

Zhao, W., D. A. Yuen, and S. Honda (1992), Multiple phase transitions and the style of mantle convection, *Physics of the Earth and Planetary Interiors*, *72*(3-4), 185–210, doi: http://doi.org/10.1016/0031-9201(92)90201-6.